DOE/ID/12079-5

TOPICAL REPORT

CONTROLLED-SOURCE AUDIOMAGNETOTELLURICS IN GEOTHERMAL EXPLORATION

By

Stewart K. Sandberg and

Gerald W. Hohmann

Work performed under Contract No.

DE-AC07-80ID12079

Department of Geology and Geophysics

University of Utah

Salt Lake City, Utah (USA)

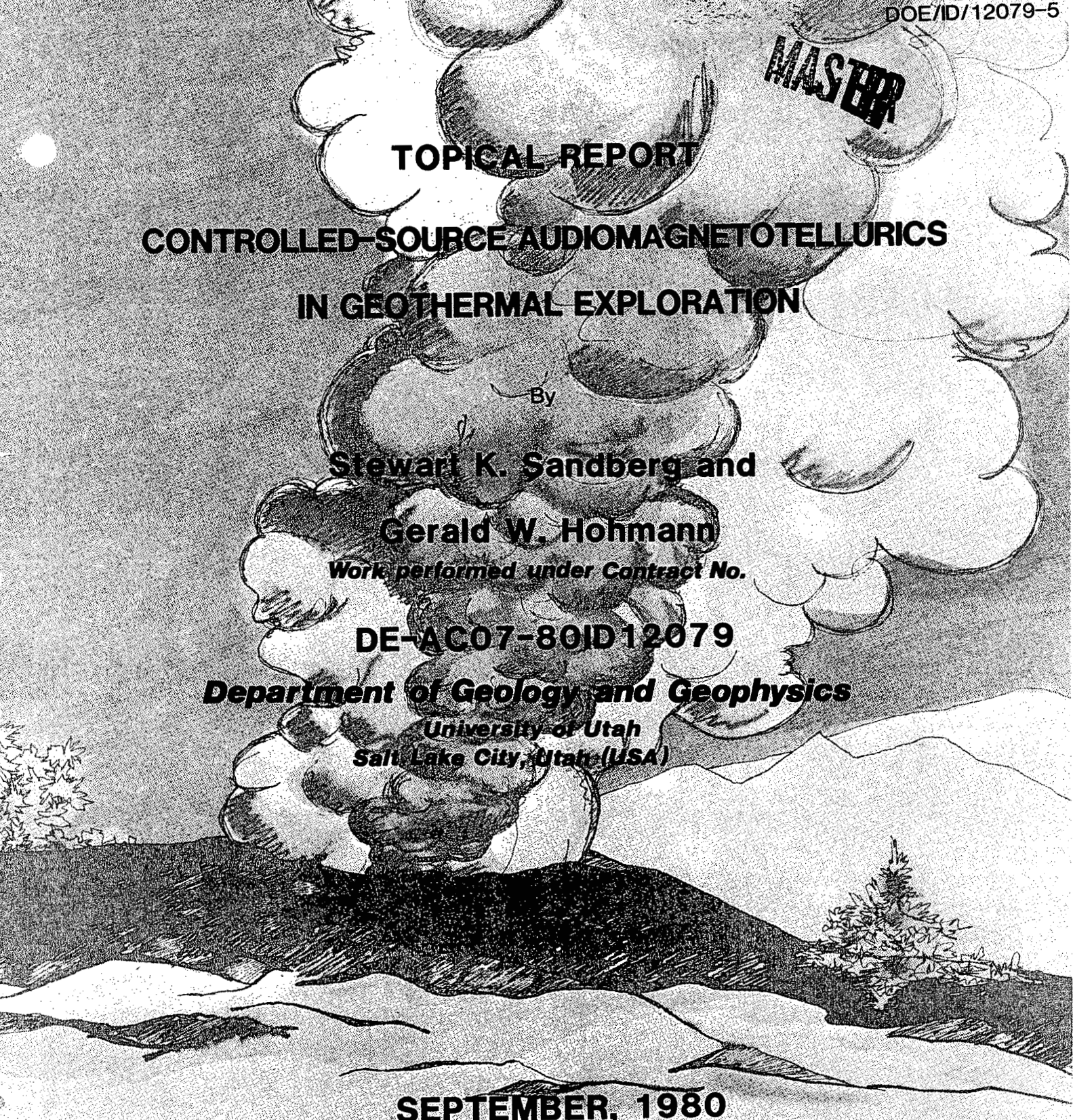

SEPTEMBER, 1980

Prepared for

DEPARTMENT OF ENERGY

Division of Geothermal Energy

DISCLAIMER

DOE/ID/12079-5

TOPICAL REPORT

CONTROLLED-SOURCE AUDIOMAGNETOTELLURICS IN GEOTHERMAL EXPLORATION

by

Stewart K. Sandberg

and

Gerald W. Hohmann

Work performed under Contract No.

DE-AC07-80ID12079

Department of Geology and Geophysics

The University of Utah

September, 1980

NOTICE

This report was prepared to document work sponsored by the United States Government. Neither the United States nor its agent, the United States Department of Energy, nor any Federal employees, nor any of their contractors, subcontractors or their employees, makes any warranty, express or implied, or assumes any legal liability or responsibility for the accuracy, completeness, or usefulness of any information, apparatus, product or process disclosed, or represents that its use would not infringe privately owned rights.

NOTICE

Reference to a company or product name does not imply approval or recommendation of the product by the University of Utah or the U.S. Department of Energy to the exclusion of others that may be suitable.

ABSTRACT

Theoretical and field tests indicate that the controlled-source audiomagnetotelluric (CSAMT) method provides an efficient means of delineating the shallow resistivity pattern above a hydrothermal system. Utilizing a transmitter overcomes the main limitation of conventional AMT: variable and unreliable natural source fields. Reliable CSAMT measurements can be made with a simple scalar receiver.

Our calculations for a half-space show that the plane wave assumption is valid when the transmitter is more than 3 skin depths away in the broadside configuration and more than 5 skin depths away in the collinear configuration. Three dimensional numerical modeling results for a bipole source 5 skin depths away compare well with those for a plane wave source, showing that the method is valid. Comparisons between 2D and 3D model results show that a 2D MT program can be used to interpret CSAMT data.

A CSAMT survey at the Roosevelt Hot Springs KGRA produced apparent resistivity contour maps at four frequencies: 32, 98, 977, and 5208 Hz. These maps show the same features as a first-separation dipole-dipole resistivity map. We also collected detailed CSAMT data at 10 frequencies on two profiles. Two-dimensional MT modeling (TM mode) of the resulting pseudosections yields models similar to those derived by modeling the dipole-dipole resistivity data. However, CSAMT resolved details not shown by the resistivity modeling. Thus

increased resolution along with an efficient field procedure makes CSAMT an attractive tool for geothermal exploration.

TABLE OF CONTENTS

LIST OF FIGURES

LIST OF TABLES

ACKNOWLEDGMENTS

We wish to thank Kennecott Copper Corp. for providing the receiver used in the fieldwork. Technical advice and assistance was gratefully received from W. SanFilipo, W. Petrick, P. Wannamaker and J. Stodt. We also wish to thank S. H. Ward for critically reviewing the manuscript. This work was supported under DOE contract number DE-AC07-80ID12079.

INTRODUCTION

Dipole-dipole resistivity and scalar audiomagnetotelluric (AMT) surveys frequently are conducted to delineate the shallow resistivity pattern above a hydrothermal system. The former method is slow and expensive, while the latter is not dependable. Natural fields in the AMT band (10-10^4 Hz) are due to thunderstorm energy propagating in the earth-ionosphere cavity; therefore the source fields at certain times of the day or in certain seasons may be so weak that it is impossible to obtain reliable data. Furthermore, tensor measurements are required, because the source field direction varies with time. These limitations can be overcome by utilizing a controlled source: a grounded wire driven at one or several frequencies and located far enough away so that the incident field at the receiver approximates a plane wave.

Strangway, et al., (1973) discuss the application of natural-field AMT in mineral exploration. Hoover, et al., (1976), Hoover and Long (1976), Hoover, et al., (1978) and Long and Kaufman (1980) describe reconnaissance natural-field AMT investigations with station spacings of several kilometers in geothermal areas. However, in geothermal exploration AMT may be most useful for detailed mapping of near-surface low resistivity zones due to rock alteration and saline pore fluids.

Goldstein and Strangway (1975) introduced the use of a

controlled-source for AMT surveys, and discussed applications in mineral exploration. If the source is several skin depths from the observation point, the electromagnetic field behaves as a plane wave, and the conventional magnetotelluric formula for apparent resistivity can be used to reduce the data.

In this paper we investigate the validity of the plane wave approximation for half-space and three-dimensional (3D) models. Then we describe the results and interpretation of a CSAMT survey at the Roosevelt Hot Springs KGRA (Known Geothermal Resource Area) in Utah.

PLANE WAVE APPROXIMATION

We derived expressions for the magnetic and electric fields due to an infinitesimal grounded electric dipole over a halfspace using TM and TE potentials. The results are not presented here since solutions have been published elsewhere (for example, see Goldstein and Strangway, 1975). The infinitesimal dipole solution was then numerically integrated over a finite length source to more accurately simulate a field situation. Solutions were calculated over a 3-1/4 (5.23 km) by 3-1/4 (5.23 km) mile grid for a 2000 (609.6m) ft transmitter, a half-space resistivity of 100 ohm-m, and a frequency of 32.02 Hz.

AMT scalar apparent resistivities are calculated according to the relation:

$$\rho_a = \frac{1}{\mu\omega}\left(\frac{|E|}{|H|}\right)^2$$

where E and H are perpendicular horizontal electric and magnetic field components, respectively. For our half-space model, the transmitter bipole is oriented along the x-axis.

Figure 1 shows apparent resistivities calculated using the component of the electric field parallel to the transmitter. For reference, distances of 3, 4, and 5 skin depths, δ ($\delta = \sqrt{\frac{2}{\mu\omega\sigma}}$) are shown. Apparent resistivities are within ten percent of the true half-space resistivity (100 ohm-m) when measured more than three skin

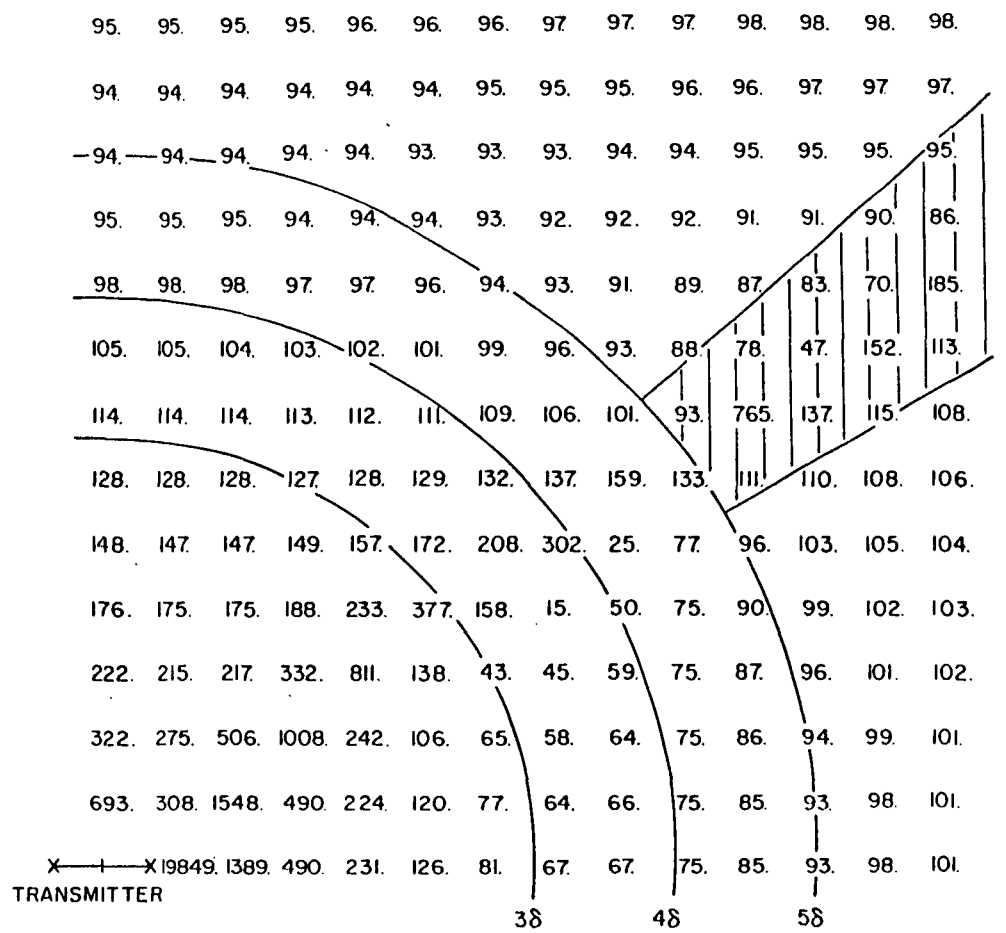

Figure 1. Apparent resistivities calculated using E_x and H_y with the transmitter bipole parallel to the x-axis. Station spacing = 1/4 mi (402.34 m), transmitter bipole = 2000 ft (609.6 m), halfspace resistivity = 100 ohm-m, frequency = 32.02 Hz, skindepth (δ) = 884 m (.55 mi). Three, four, and five skin depth distances from the center of the transmitter are shown. The shaded area is the region of minimum coupling.

depths broadside to the transmitter, and more than five skin depths collinear with the transmitter. The broadside configuration refers to orienting the electric field receiving dipole parallel to the transmitter bipole, and on its center line. Collinear refers to orienting parallel to the transmitter bipole and on its axis. However, resistivities in the shaded region of Figure 1, although far enough away, are not within ten percent of 100 ohm-m, because the electric and magnetic fields are almost perpendicular to the measuring directions.

Orientations of the major axes of the electric and magnetic field polarization ellipses are plotted in plan view in Figures 2 and 3, respectively. The shaded areas in these figures correspond to the minimum coupling area in Figure 1. Note that in the shaded areas E_x and H_y, the field components used in the apparent resistivity calculations of Figure 1, are small. Apparent resistivities calculated using these small inaccurate components are erratic; the same would be true of field data. Goldstein and Strangway (1975) show similar regions of minimum coupling on apparent resistivity grids from an infinitesimal electric dipole source.

Figure 4 shows apparent resistivities calculated using the component of the electric field perpendicular to the transmitter bipole. At distances from the transmitter greater than three skin depths, calculated apparent resistivities are everywhere within ten percent of the true half-space resistivity. Minimum coupling in this orientation occurs along the x- and y-axes (with the transmitter on the x-axis, centered at the origin).

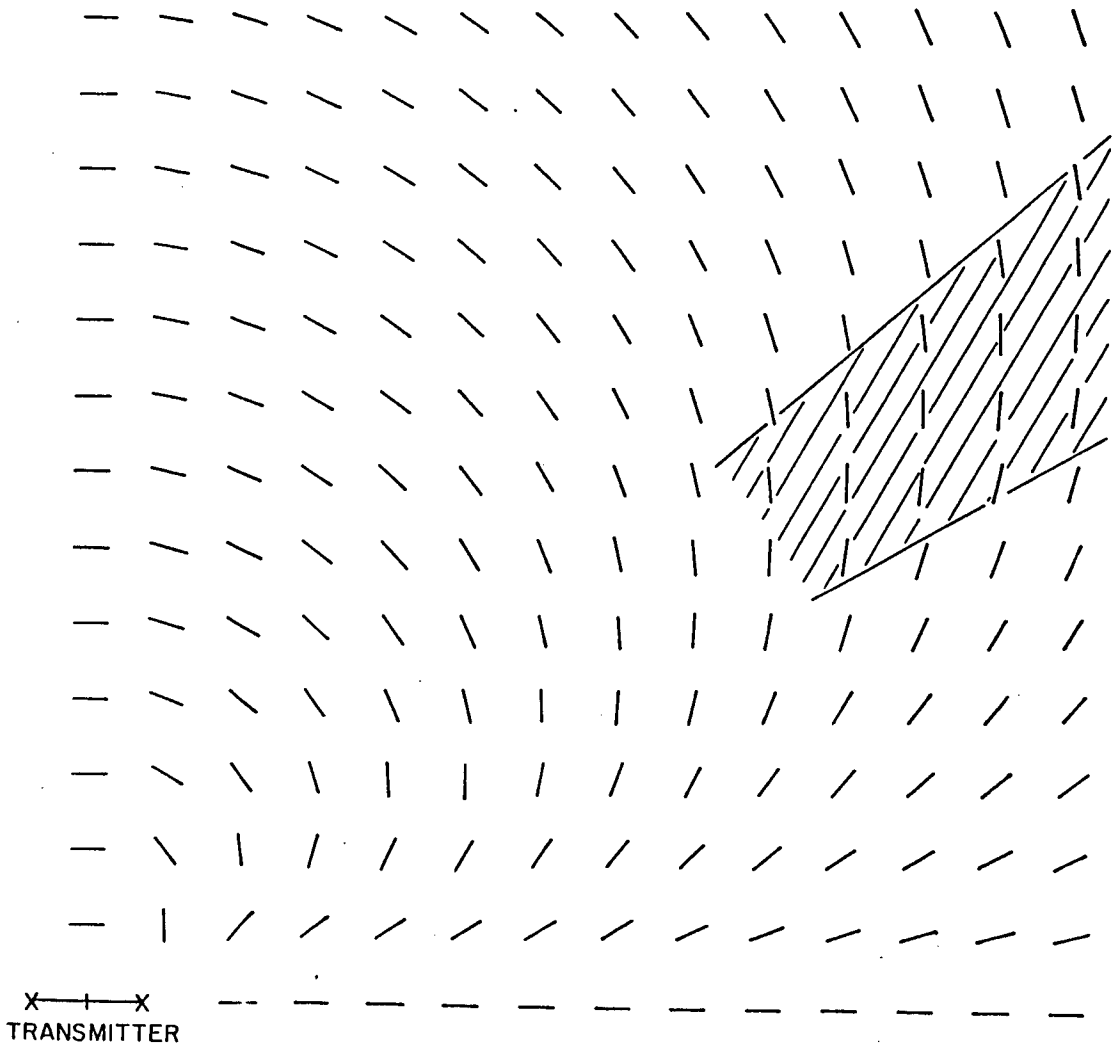

Figure 2. Orientations of the major axes of the electric field polarization ellipses. The shaded area is the same as that in Figure 1.

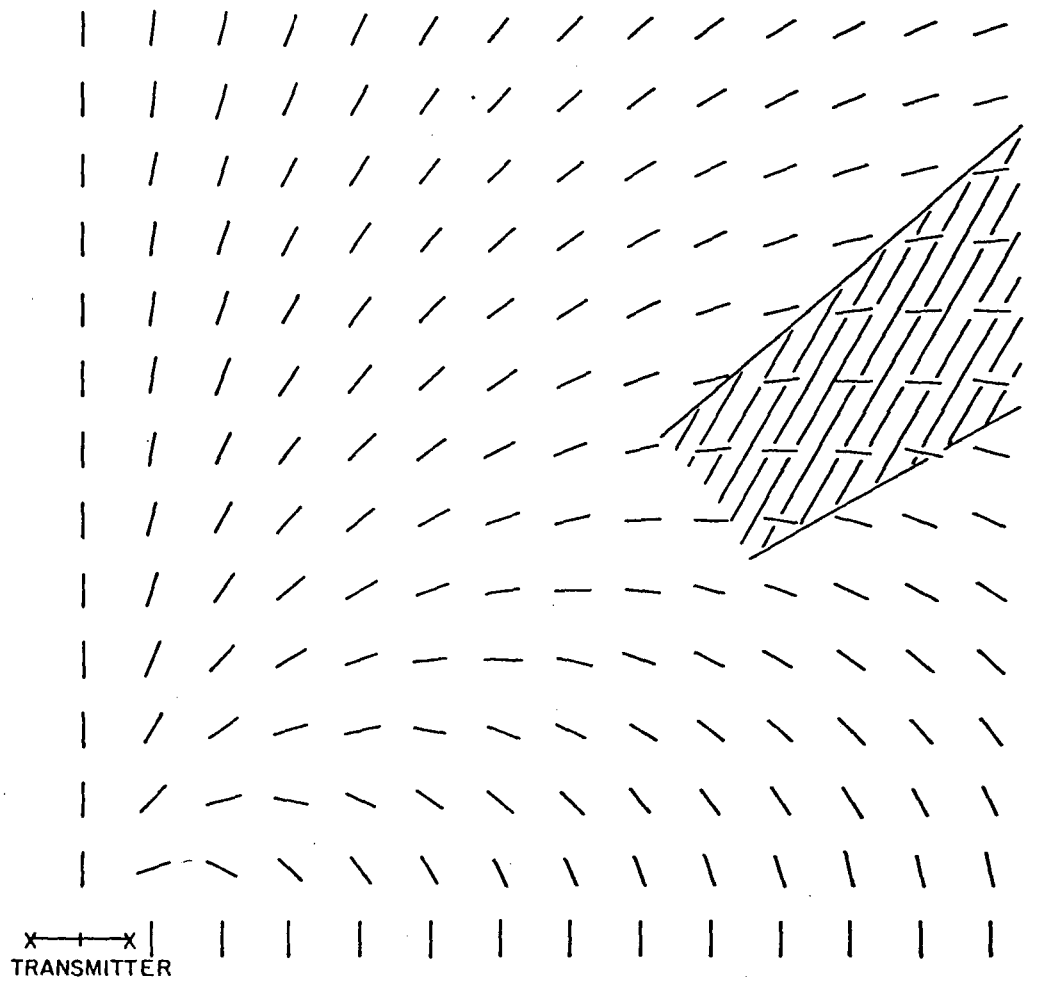

Figure 3. Orientations of the major axes of the magnetic field polarization ellipses. The shaded area is the same as that in Figure 1.

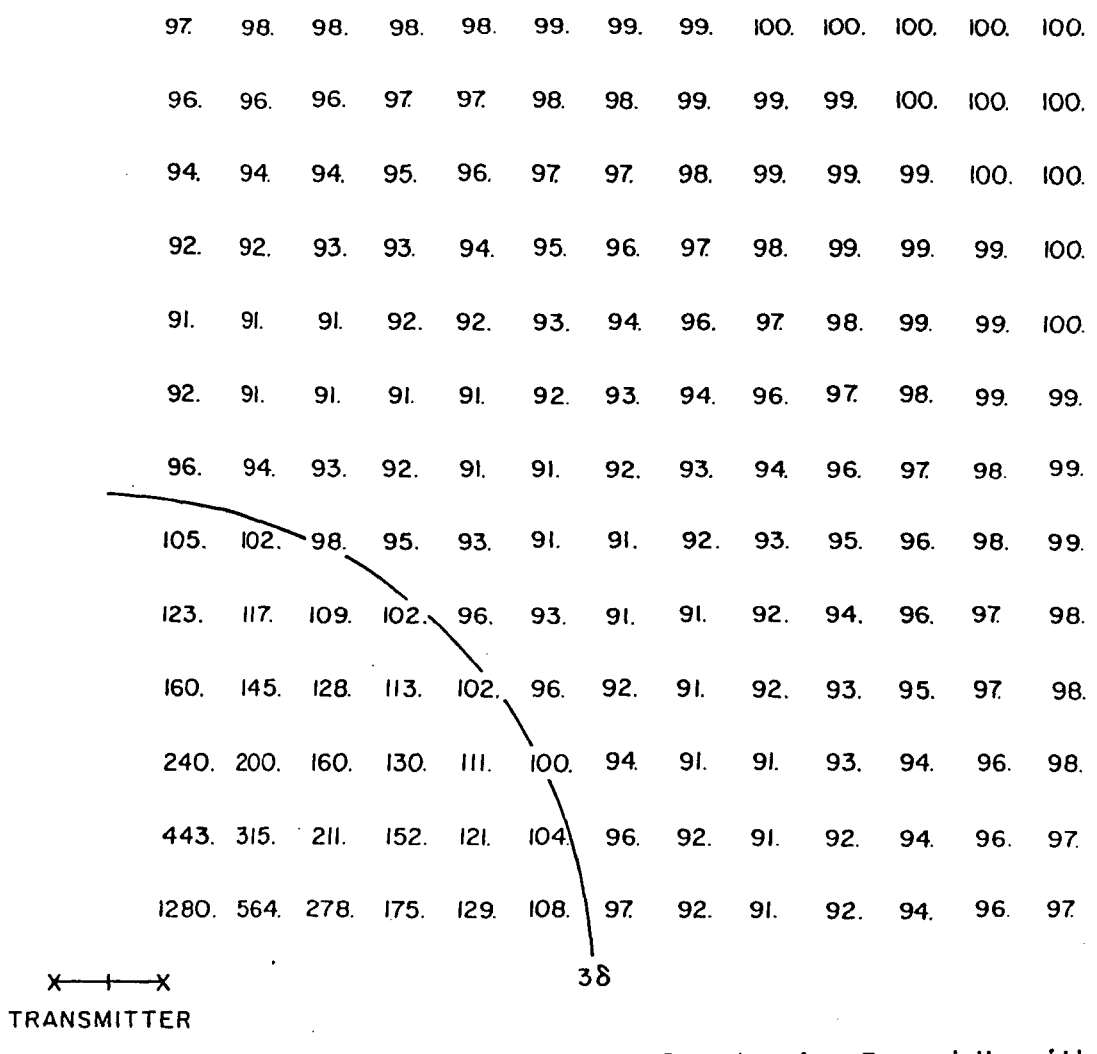

Figure 4. Apparent resistivities calculated using E_y and H_x with the transmitter bipole parallel to the x-axis. Three skindepths distance from the center of the transmitter is shown.

Profiling parallel to the transmitter bipole (broadside configuration) will require measuring electric and magnetic fields in directions which are not maximum coupling orientations. A profile along a radial path perpendicular to or collinear with the bipole will preserve maximum coupling along the entire profile, and is therefore recommended.

Kan and Clay (1979) show half-space solutions for the fields within the earth using a dipole transmitter and state that the plane wave source approximation is valid beyond about six skin depths. Their results are based on phases of the fields in the earth.

Three-dimensional (3D) modeling was employed to simulate the CSAMT technique in the general case, and to check the plane wave approximation for an inhomogeneity in a half-space. The program modeled a bipole source on a 3D earth using an integral equation solution (Hohmann, 1975) modified for a symmetric body using group theoretic concepts (Tripp and Hohmann, 1980) to reduce computer time. A similar program simulated a plane wave source over the same 3D earth for comparison. The 3D earth consisted of a homogeneous half-space in which a conductive rectangular prism 300 x 600 x 50 m thick was buried 50 m deep. The frequency was 100 Hz, the halfspace resistivity was 100 ohm-m, and the prism resistivity was 10 ohm-m.

The first source was located approximately five skin depths from the body, representing a transmitter-receiver separation adequate for the broadside configuration, and just large enough for the collinear configuration. Figure 5a shows a plan map of apparent resistivities calculated on profiles across the buried prism using E_x and H_y

Figure 5. Plan view of apparent resistivities over a buried 3D prism calculated using E_x and H_y. Due to the symmetry, only half of the area is shown. Prism resistivity = 10 ohm-m, background halfspace resistivity = 100 ohm-m, frequency = 100 Hz. (a) Transmitter bipole in collinear configuration centered at x = 2900 m. (b) Plane wave source with the electric field polarized in the x-direction. A profile of data along y = 600 m has been added in (a) to constrain the apparent resistivity contours.

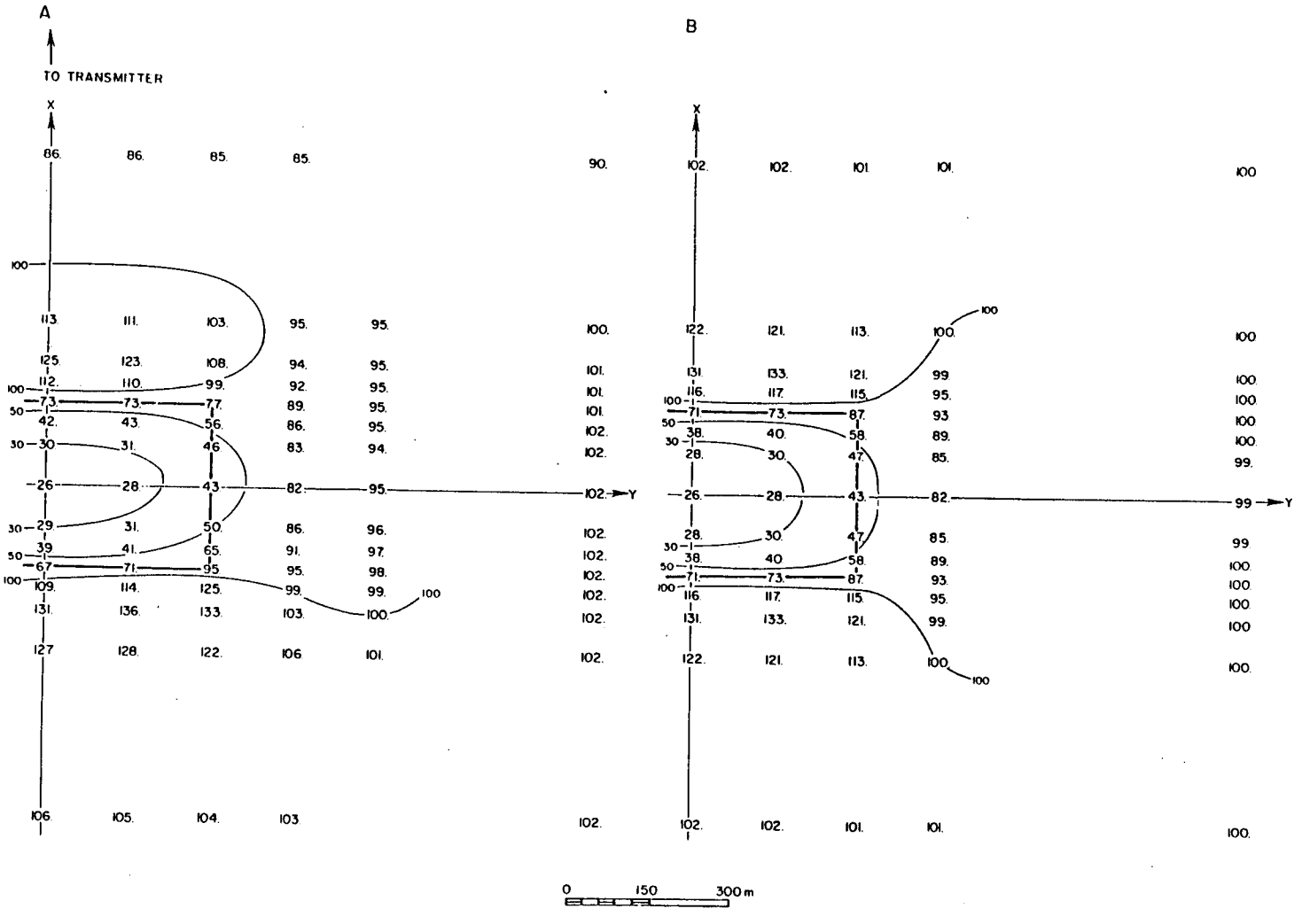
A
TO TRANSMITTER
X
B
X
Y
Y
0
150
300 m

with transmitter electrodes located at 2600 and 3200 m from the origin on the x-axis. The nearest source electrode is 4.9 skin depths from the nearest edge of the body, and the geometry corresponds to the collinear configuration.

In Figure 5b, apparent resistivities are calculated in the same manner except the source is a plane wave with the electric field polarization in the x-direction. A comparison of Figures 5a and 5b shows the validity of the plane wave approximation for an inhomogeneous earth. Discrepancies are larger on the source side of the body because it is closer to the transmitter bipole.

Figure 6a shows apparent resistivities calculated from E_y and H_x for transmitter electrodes centered 2900 meters from the origin in the x-direction (5.8 skin depths from the center of the prism) and parallel to the y-axis, i.e. the broadside configuration. For comparison, Figure 6b shows apparent resistivities for a plane wave source with the electric field in the y-direction. There is good agreement, showing that the source is sufficiently far away that the plane wave approximation is valid.

Profiles of apparent resistivity along the x-axis for both transmitter orientations are compared with two-dimensional MT finite element modeling results in Table 1 over a body with the same cross section as the one used in the 3D modeling. The similarity between the CSAMT profiles and the 2D MT profiles indicates that the CSAMT profiles could have been interpreted accurately with 2D MT modeling. Also, referring to Figures 5a, 5b, 6a, and 6b, the profile need not have passed directly over the center of the body, since the apparent

Figure 6. Plan view of apparent resistivities over a buried 3D prism calculated using E_y and H_x. (a) Transmitter bipole in broadside configuration centered at x = 2900 m. (b) Plane wave source with the electric field polarized in the y-direction. A profile of data along y = 600 m has been added in (a) to constrain the apparent resistivity contours.

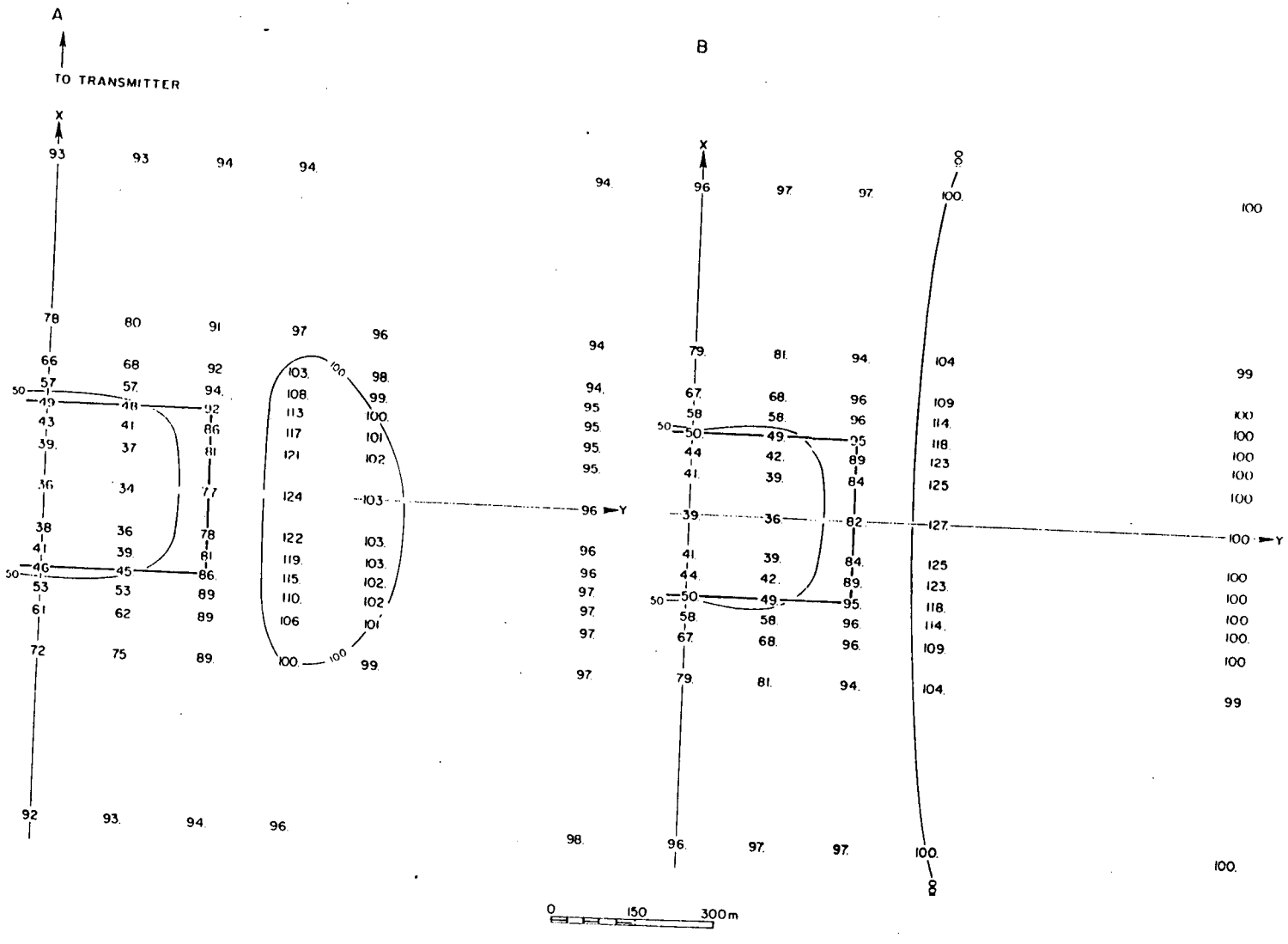
A
TO TRANSMITTER
X
B
X
Y
Y
0
150
300m

Table 1. A comparison of apparent resistivities for a profile over the center of a buried 3D prism. The 3D MT and 2D MT sources are plane waves with the source polarization in the same direction as the field components measured. The CSAMT sources are broadside and colliear bipoles centered 2900 m from the center of the profile in the positive x-direction. Profile (a) uses field components E_x and H_y in apparent resistivity calculations, and (b) uses E_y and H_x.

a.

x-coordinate	3D MT	2D MT	CSAMT
-600 m	102 Ω-m	102 Ω-m	106 Ω-m
-300	122	119	127
-225	131	129	131
-185	116	119	109
-150	71	78	67
-115	38	39	39
-75	28	25	29
0	26	22	26
75	28	25	30
115	38	39	42
150	71	78	73
185	116	119	112
225	131	129	125
300	122	119	113
600	102	102	86

b.

x-coordinate	3D MT	2D MT	CSAMT
-600 m	96 Ω-m	96 Ω-m	92 Ω-m
-300	79	80	72
-225	67	69	61
-185	58	61	53
-150	50	53	46
-115	44	47	41
-75	41	42	38
0	39	40	36
75	41	42	39
115	44	47	43
150	50	53	49
185	58	61	57
225	67	69	66
300	79	80	78
600	96	96	93

resistivities along y = 150 m are similar to those along the x-axis.

The effect of obtaining data too close to the transmitter was simulated by placing source electrodes on the x-axis 700 and 1300 meters from the origin in Figure 7a. Electrodes 900 meters from the origin in the x-direction and parallel to the y-axis represent the other incident field mode in Figure 7b. Both modes exhibit resistivity lows over the buried prism, but the apparent resistivities are far from the plane wave values shown in Figures 5b and 6b. The incident field does not approximate a plane wave in this case, because the distance from the center of the transmitter to the center of the body is only 1.8 skin depths.

When applying CSAMT in highly resistive terrain, the required transmitter-receiver separation may be so large that obtaining data too close to the transmitter is necessary in order to receive the signal. Such data is not interpretable quantitatively with plane wave MT modeling. Goldstein and Strangway (1975) present curves for one-dimensional interpretation of soundings taken too close to the transmitter.

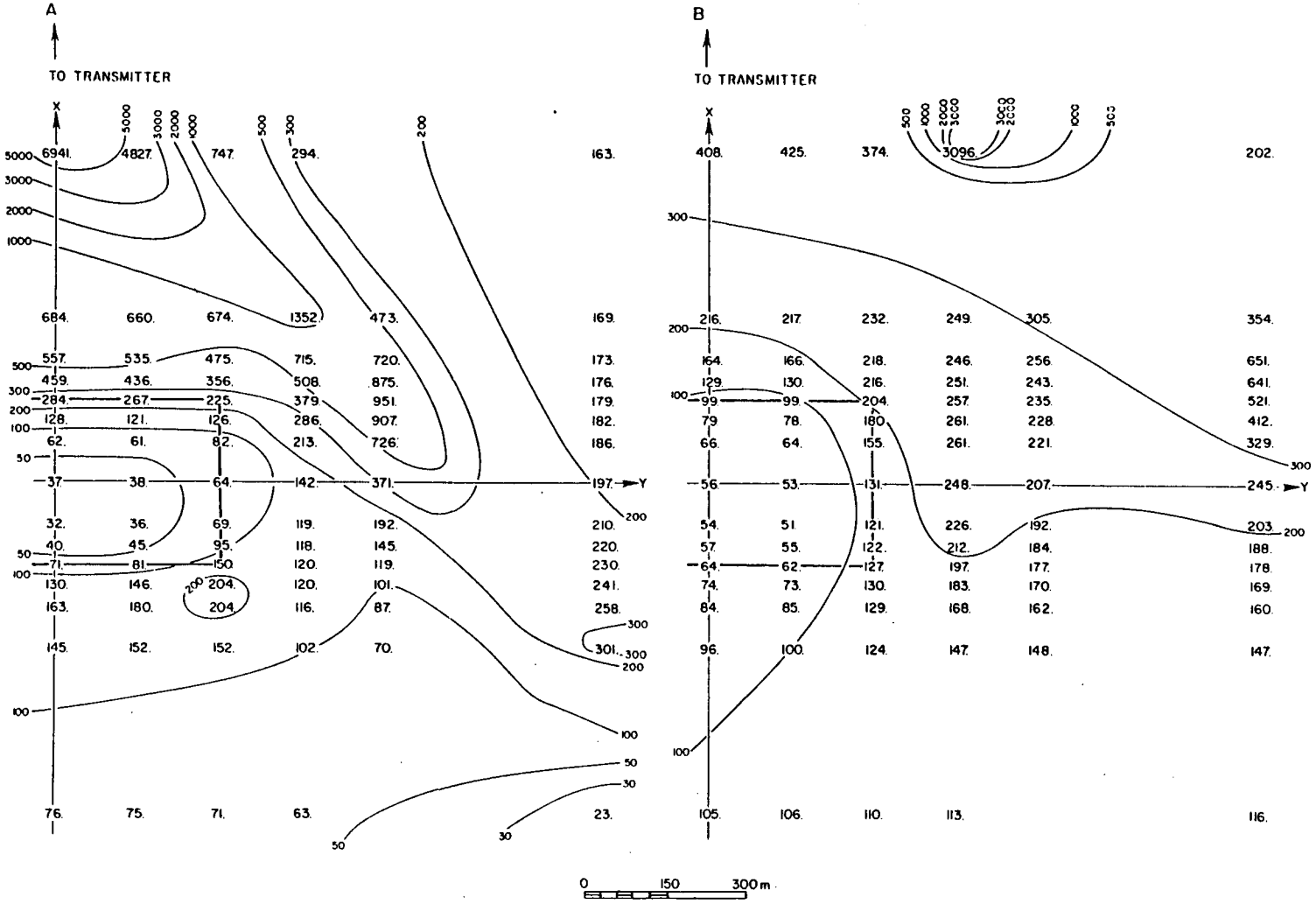

Figure 7. (a) Same as 5(a) except transmitter is centered at x = 1000 m. (b) Same as 6(a) except transmitter is centered at x = 900 m.

ROOSEVELT HOT SPRINGS CSAMT SURVEY

We carried out a CSAMT survey at Roosevelt Hot Springs KGRA during August and September 1979. The KGRA is located in Beaver County, in west-central Utah on the western margin of the Mineral Mountains. Bedrock in the area is dominated by metamorphic rocks of Precambrian age. The Mineral Mountains pluton is Tertiary with felsic plutonic phases. There is evidence for recent igneous activity in rhyolite flows, domes, and pyroclastics of Pleistocene age. The geology of the area is summarized by Nielson, et al. (1978).

The area has been studied in detail by the Department of Geology and Geophysics of the University of Utah and by the Earth Science Laboratory of the University of Utah Research Institute. A summary of the work can be found in Ward, et al. (1978). Because the area is so well documented, it is a good location for testing an exploration technique.

Roosevelt Hot Springs is a structurally controlled geothermal reservoir. Geothermal exploration targets are the faults and fractures which control the movement of fluids. Alteration products observed along these faults and fractures are associated with chemical reactions caused by the hydrothermal system. Due to the alteration minerals and the brine, the fault zones should respond as low resistivity anomalies in an otherwise moderate to high resistivity background.

The resistivity range expected is between one and a few hundred ohm-m. Formation water resistivities are in the range .52 to 2.1 ohm-m (Glenn and Hulen, 1979). Laboratory measurements on core samples from the clay alteration zone (30-60 m) in drill hole 1A near the Opal Mound fault show resistivities as low as 3-5 ohm-m (Ward and Sill, 1976).

Previous resistivity work has been done in the area by Ward and Sill (1976). A first-separation 300-m dipole-dipole resistivity contour map from their work is shown in Figure 8. They used this map along with dipole-dipole resistivity pseudosections, an aeromagnetic map, air photos, plus mapped and interpreted geology to produce a fracture map of the Roosevelt Hot Springs KGRA. Resistivity contours also were used to support a contention that brine is leaking out of the convective hydrothermal system to the north.

We carried out the CSAMT survey in two parts. First, a resistivity mapping study was completed to assess the method by comparing it with the dipole-dipole first separation resistivity map (Figure 8). The second part of the survey consisted of two east-west profiles across the low resistivity zone, with subsequent quantitative interpretation using a 2D MT modeling program.

The transmitter used in the field work was a Geotronics model EMT-5000. A Kennecott Copper Corp. scalar AMT receiver consisted of a two-channel, tunable, high-gain, narrow bandpass analog instrument which measured the logarithmic ratio of the channel inputs. A reading consisted of an electric to magnetic field ratio with no phase information.

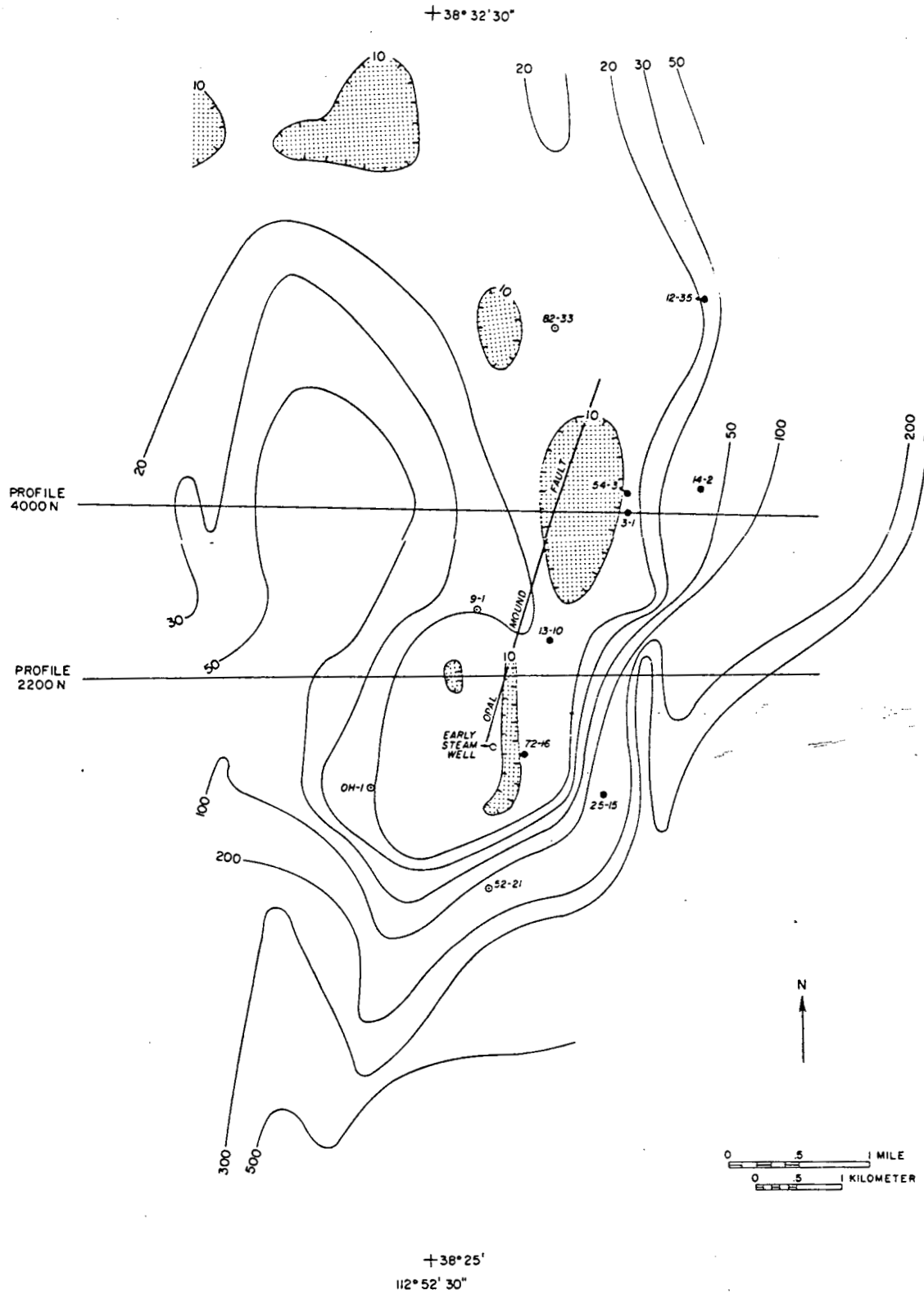

Figure 8. First separation dipole-dipole resistivity map of the Roosevelt Hot Springs KGRA (a = 300 m). After Ward and Sill (1976). Areas less than 10 ohm-m are shaded. Solid circles denote producing geothermal wells, open circles indicate non-producing wells.

The depth of exploration usually given for AMT is one skin depth. However, actual depth of exploration is somewhat less, as discussed later in this paper. In our field work, the lowest frequency was 32 Hz, so in 10 ohm-m ground the depth of exploration is less than 280m, while in 50 ohm-m ground, it is less than 628m.

Resistivity Mapping

The CSAMT procedure for resistivity mapping is based on our theoretical results. Since the frequencies utilized in CSAMT are high, skin depths are short and the effect of lateral inhomogeneities is small. The assumption of a one-dimensional, i.e. layered earth at each receiver site allows apparent resistivity calculations to be made by measuring the field in maximum coupling orientations. A transparent plot of electric field direction (Figure 2) over a half-space is constructed at the same scale as the field map. Overlaying the field direction plot helps to orient the receiver for maximum signal strength. The distance from the transmitter should be at least three skin depths, using the largest resistivity between receiver and transmitter, and the lowest frequency of the sounding. Apparent resistivities are calculated for several frequencies at each station, and a contour map is constructed for each frequency to delineate the near-surface resistivity pattern.

Field work at Roosevelt Hot Springs KGRA resulted in 136 unique stations occupied, 47 of which were located on two profiles. For resistivity mapping, apparent resistivities were measured at four frequencies: 5208, 977, 98, and 32 Hz. Two transmitter sites were

used for the reconnaissance survey, and three others were occupied for profiling. Apparent resistivity contour maps at each of the four frequencies are shown in Figures 9, 10, 11, and 12. The general contour trend and the positions of the low resistivity zones compare well with the first separation dipole-dipole resistivity map in Figure 8.

The 5208 Hz map of Figure 9 exhibits two zones of low apparent resistivity. One is located around the early steam well. The other is just west of well 3-1 and trends northwest from there through well 82-33 and northeast towards well 12-35. The low resistivities coincide with mapped near-surface alteration and brines associated with the geothermal system. These low resistivities are bounded on the east by the more resistive unaltered granitic pluton, and on the west by unaltered alluvium west of the Opal Mound. Geothermal production wells lie within or just to the east of the low-resistivity zone, and non-producing wells lie to the south and west. The 100 ohm-m contour north of well 82-33 is not due to noise in the data: high resistivities also occur here in 100 meter dipole-dipole data.

The 977 Hz map of Figure 10 defines the same general resistivity trend. A station in the northwest part of the map has a low apparent resistivity of 15 ohm-m. This low resistivity area broadens and becomes more defined in the maps of apparent resistivity for the lower frequencies. Prehistoric Lake Bonneville sediments occur in this area (Ward and Sill, 1976) and explain this feature. The northern low-resistivity zone along the Opal Mound fault extends farther northwest at this frequency. This could indicate that the geothermal

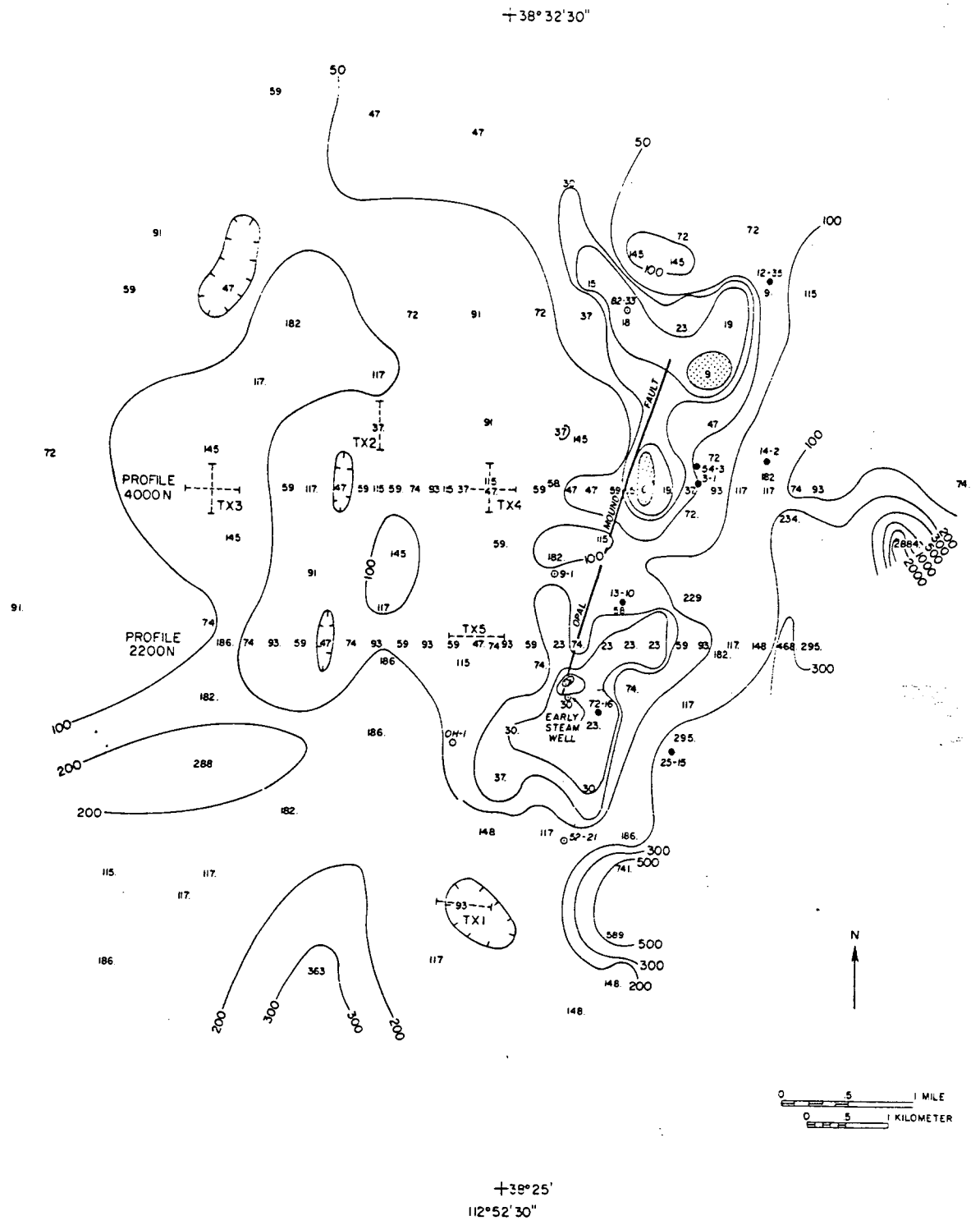

Figure 9. CSAMT apparent resistivity map of Roosevelt Hot Springs KGRA. Frequency = 5208 Hz. Areas less than 10 ohm-m are shaded.

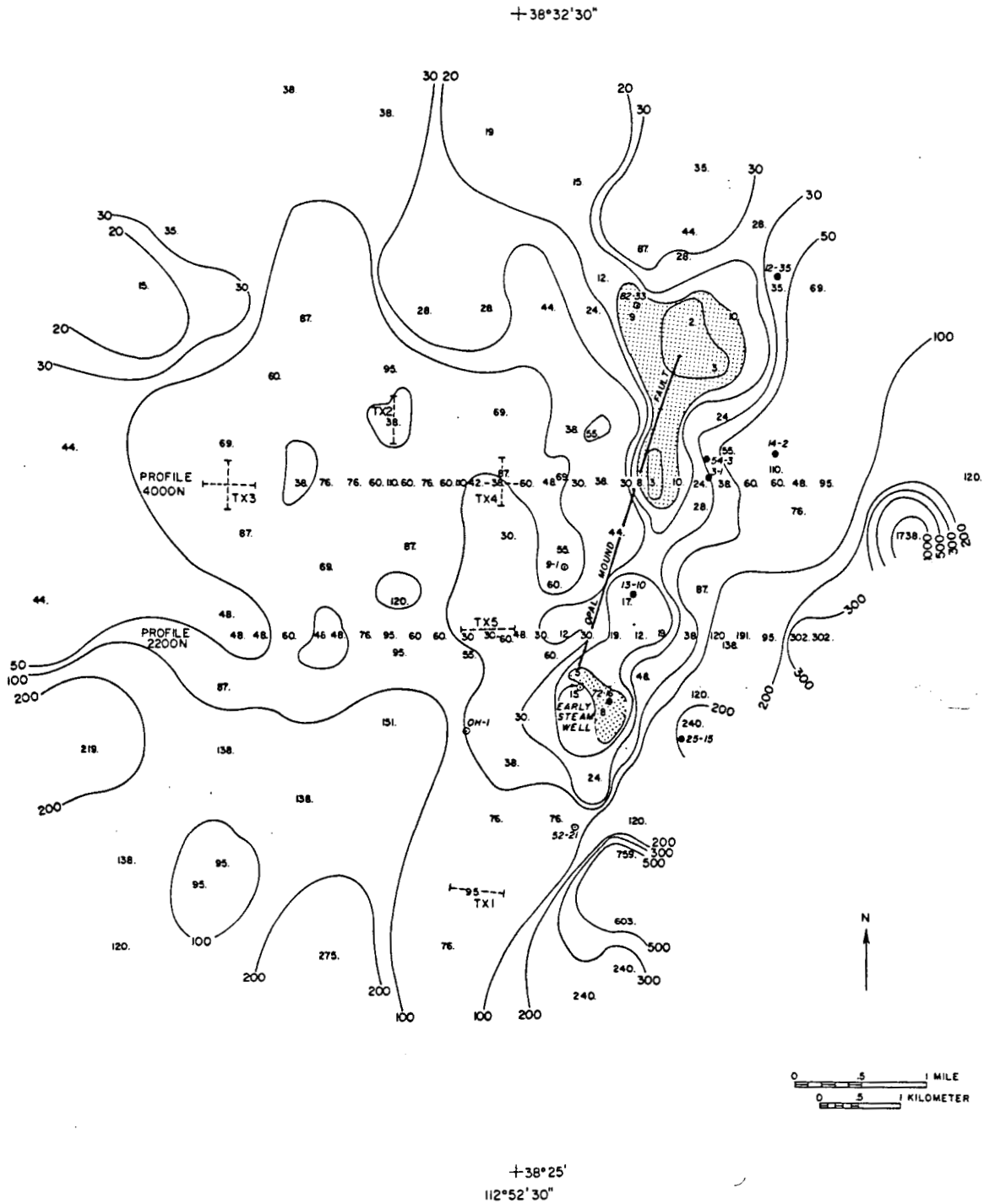

Figure 10. CSAMT apparent resistivity map of Roosevelt Hot Springs KGRA. Frequency = 977 Hz. Areas less than 10 ohm-m are shaded.

system is leaking or has leaked to the northwest.

The 97.7 Hz map of Figure 11 shows low resistivity zones larger in area, with the northern zone extending due north. The conductive zone to the northwest is well defined.

The 32.02 Hz map of Figure 12 shows bedrock to the east and southeast indicated by the high apparent resistivity values. Conductive zones correspond to the geothermal areas as well as the Lake Bonneville sediments to the northwest. The conductive zone along 2200N at the Opal Mound fault is enlarged to the west at this frequency possibly indicating westward brine leakage from the fault.

The absolute accuracy of the resistivities obtained by our equipment was checked by re-occupying a magnetotelluric site obtained in an earlier survey. CSAMT data agree with the MT data, indicating that our equipment was working properly and apparent resistivities are accurate.

In order to determine the reliability of the data obtained in the survey, we repeated several stations. The repeatability was usually within one decibel of the E/H ratio read from the receiver (One decibel greater corresponds to multiplying the apparent resistivity by 1.26 and one decibel less yields apparent resistivity divided by 1.26). Two receiver and coil sets were used; ratio differences between the two different sets usually were within one decibel of each other. These accuracy and repeatability tests are explained in more detail in Appendix F.

A CSAMT resistivity mapping survey appears to be more efficient than conventional dipole-dipole resistivity mapping. The CSAMT

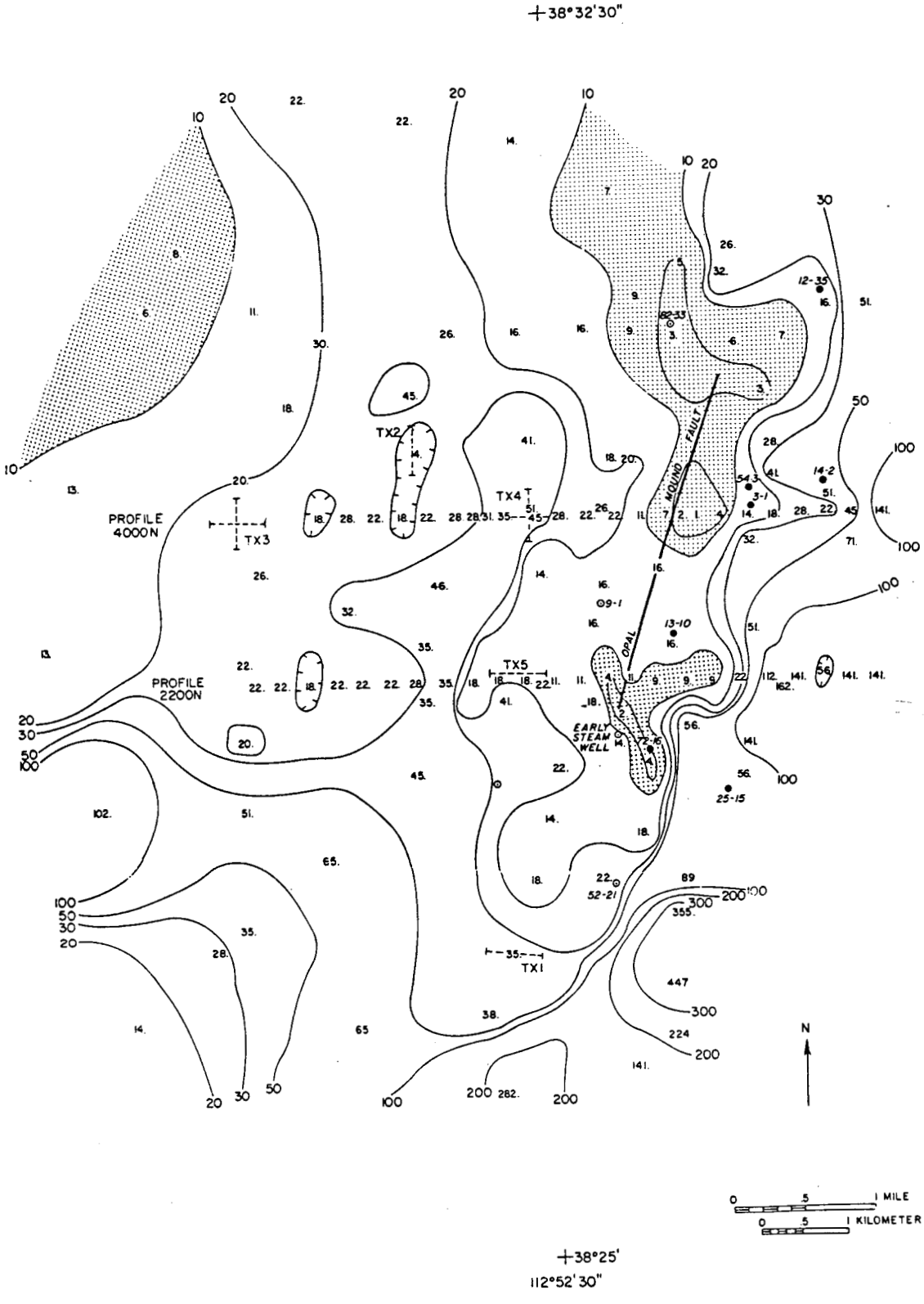

Figure 11. CSAMT apparent resistivity map of Roosevelt Hot Springs KGRA. Frequency = 98 Hz. Areas less than 10 ohm-m are shaded.

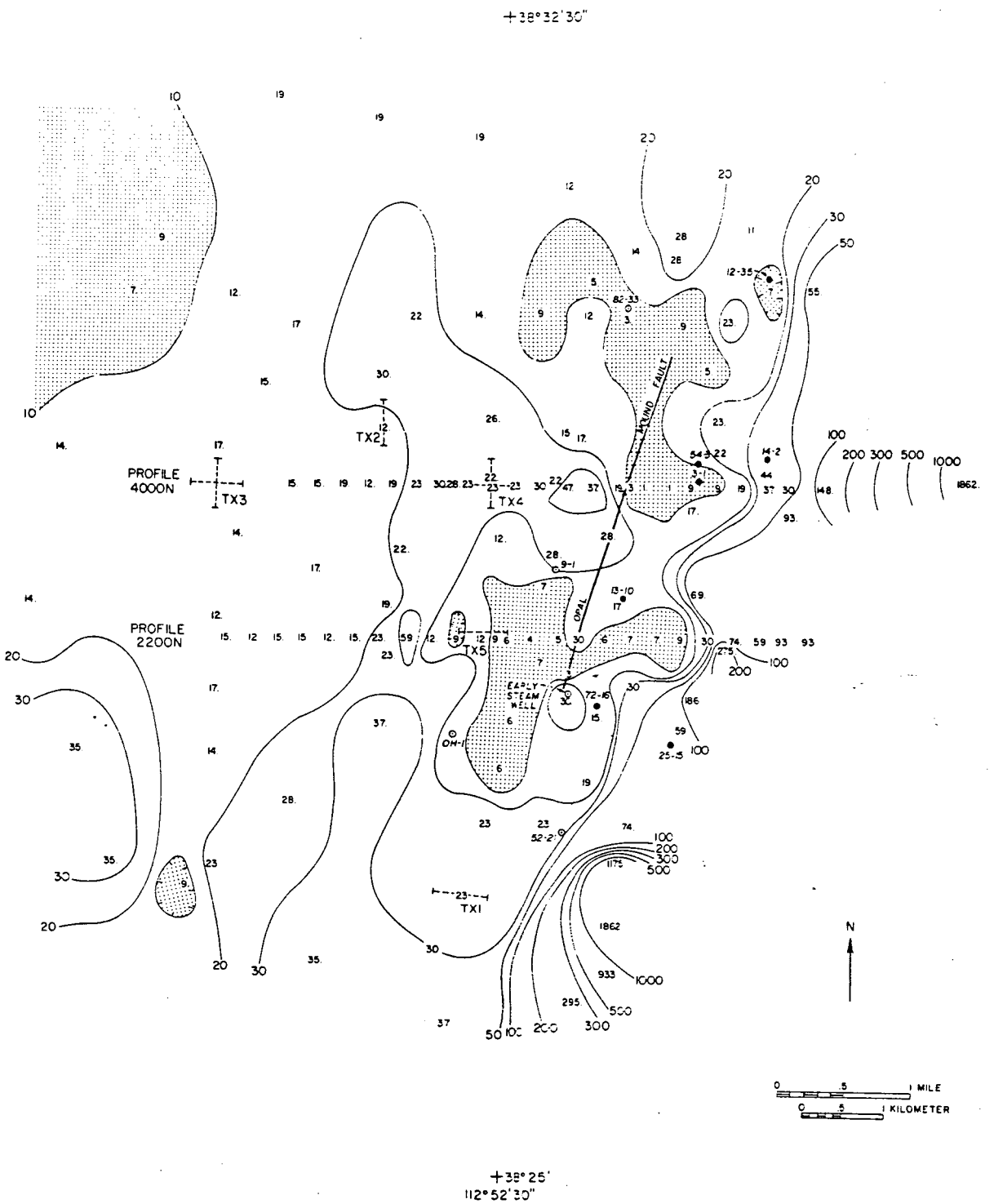

Figure 12. CSAMT apparent resistivity map of Roosevelt Hot Springs KGRA. Frequency = 32 Hz. Areas less than 10 ohm-m are shaded.

receiver only requires a 30-m wire for the electric field sensor, and a portable coil for detecting the magnetic field, instead of several hundred meters of wire as in the dipole-dipole resistivity procedure. We found that a CSAMT station could be read in about 15 minutes, including set-up. Also, since the technique doesn't require being confined to profiles, as in the case of dipole-dipole resistivity, rapid areal coverage is possible using existing roads.

The similarity between the CSAMT maps and the first separation dipole-dipole resistivity map, along with the reoccupied MT site results and repeatability tests, indicate that these data are accurate enough for quantitative interpretation. We ran two profiles across the low resistivity zone and modeled the results. The locations of the profiles are shown in Figure 9.

Profile One

Profile one is an east-west traverse along dipole-dipole resistivity line 4000N (Figure 8). The CSAMT station spacing was 300 m, and two transmitter locations, labeled TX3 and TX4 in Figure 9 were used. The transmitter consisted of an orthogonal pair of 2000 ft (609.6 m) bipoles allowing apparent resistivity measurements with the electric field perpendicular and parallel to the traverse. Two sets of data were thereby obtained, corresponding to electric field orientations perpendicular (TM) and parallel (TE) to geologic strike. The two sets of data are plotted as pseudosections in Figures 13 and 14.

One-dimensional MT inversion of the TM mode data at each station

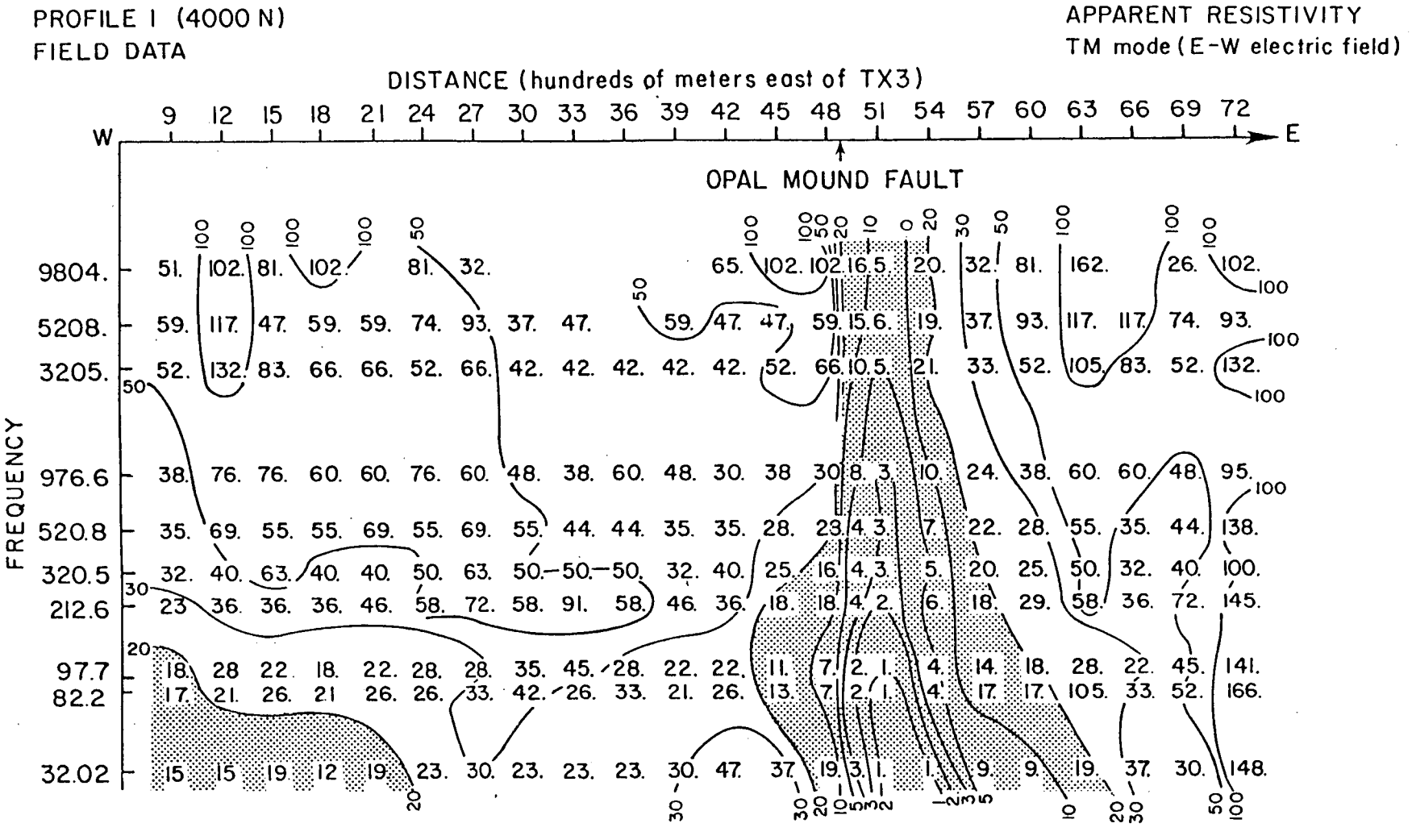

Figure 13. TM mode field data pseudosection from Profile One (4000 N). Apparent resistivity less than 20 ohm-m is shaded.

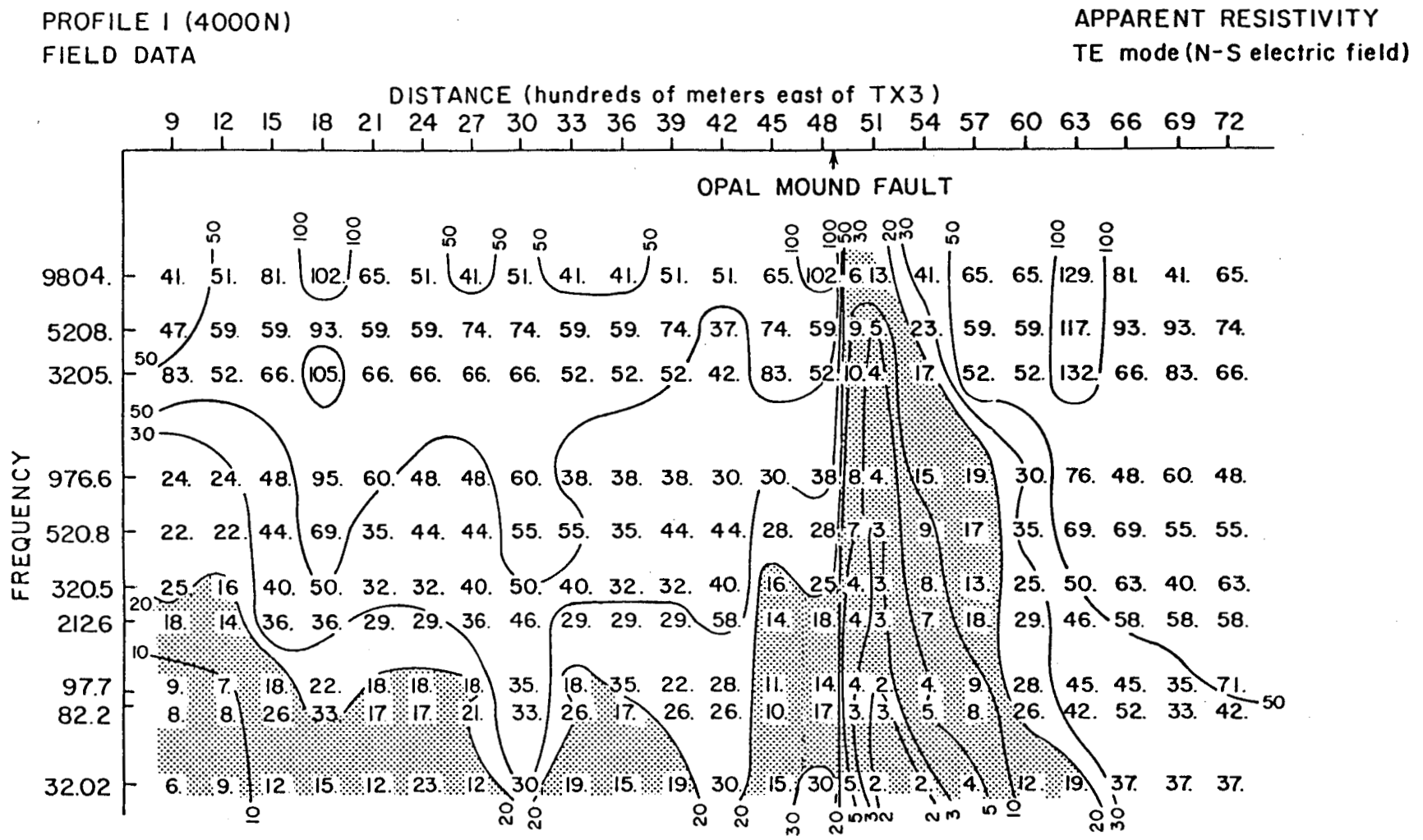

Figure 14. TE mode field data pseudosection from Profile One (4000 N). Apparent resistivity less than 20 ohm-m is shaded.

along the profile resulted in an initial two-dimensional resistivity model for the line. This model was then refined by applying a two-dimensional MT finite element forward computer program (Stodt, 1978), and adjusting the model to fit the field data. The resulting model is shown in Figure 15 next to a two-dimensional resistivity model for the same line (Ross et al., 1980) derived from combined 100 and 300 m dipole-dipole ($n \leq 4$) data (Ward and Sill, 1976). Theoretical AMT pseudosections for the CSAMT and resistivity models are shown in Figures 16 and 17, respectively. These theoretical pseudosections can be compared with the field data in Figure 13. The resistivity model response (Figure 17) doesn't fit the low frequency data very well, and apparent resistivities in the conductive area are not low enough.

A two-dimensional finite element forward dipole-dipole resistivity computer program (Killpack and Hohmann, 1979) was used to generate resistivity data from the CSAMT model. A comparison of this theoretical data and the resistivity field data is shown in Figure 18.

The dipole-dipole resistivity data in Figure 18 indicates a resistive overburden from CSAMT station 3900 to the west end of the profile. Lack of high frequency data at stations 2100, 3000, 3300, 3600, and 3900 (Figure 13) along with probable noise at the high-frequency reading at station 2700 contribute to not detecting this structure with CSAMT. The CSAMT model (Figure 15) was constructed to fit the field data, and therefore doesn't show a resistive overburden.

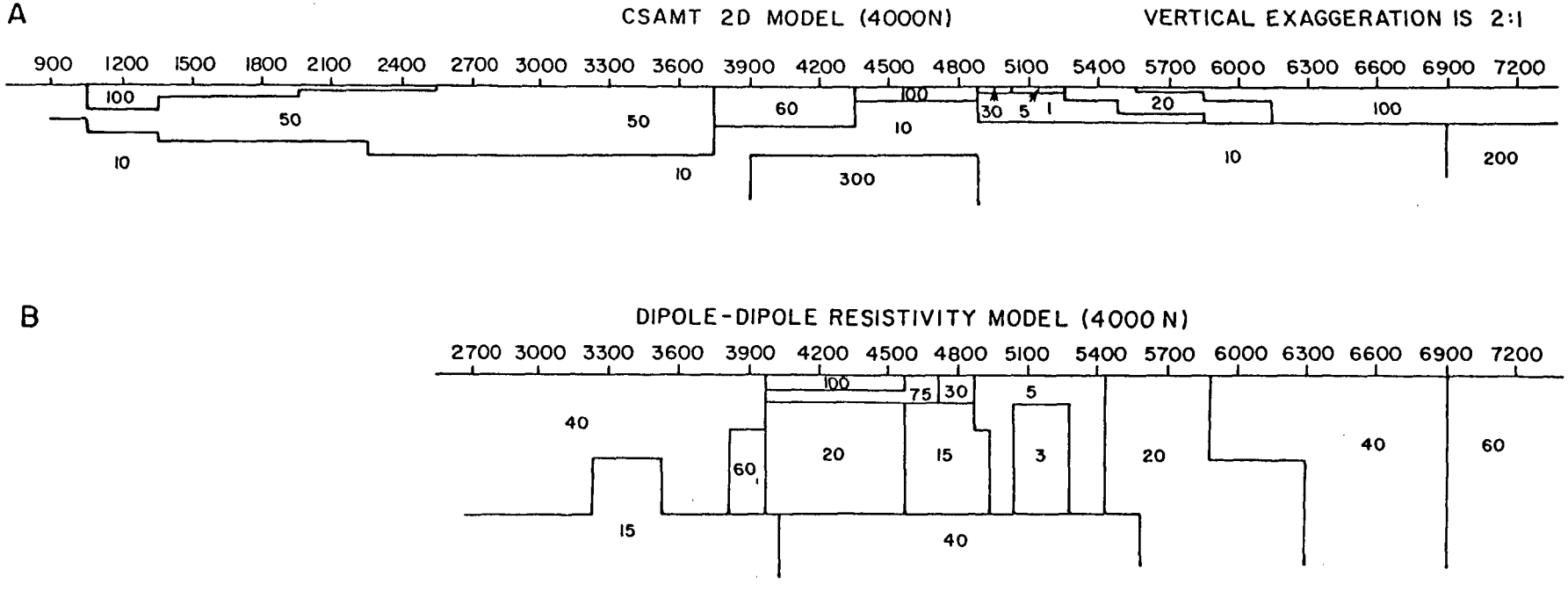

Figure 15. (a) Two-dimensional CSAMT and (b) dipole-dipole resistivity (based on 100 m and 300 m dipoles) interpretations of Profile One (4000 N).

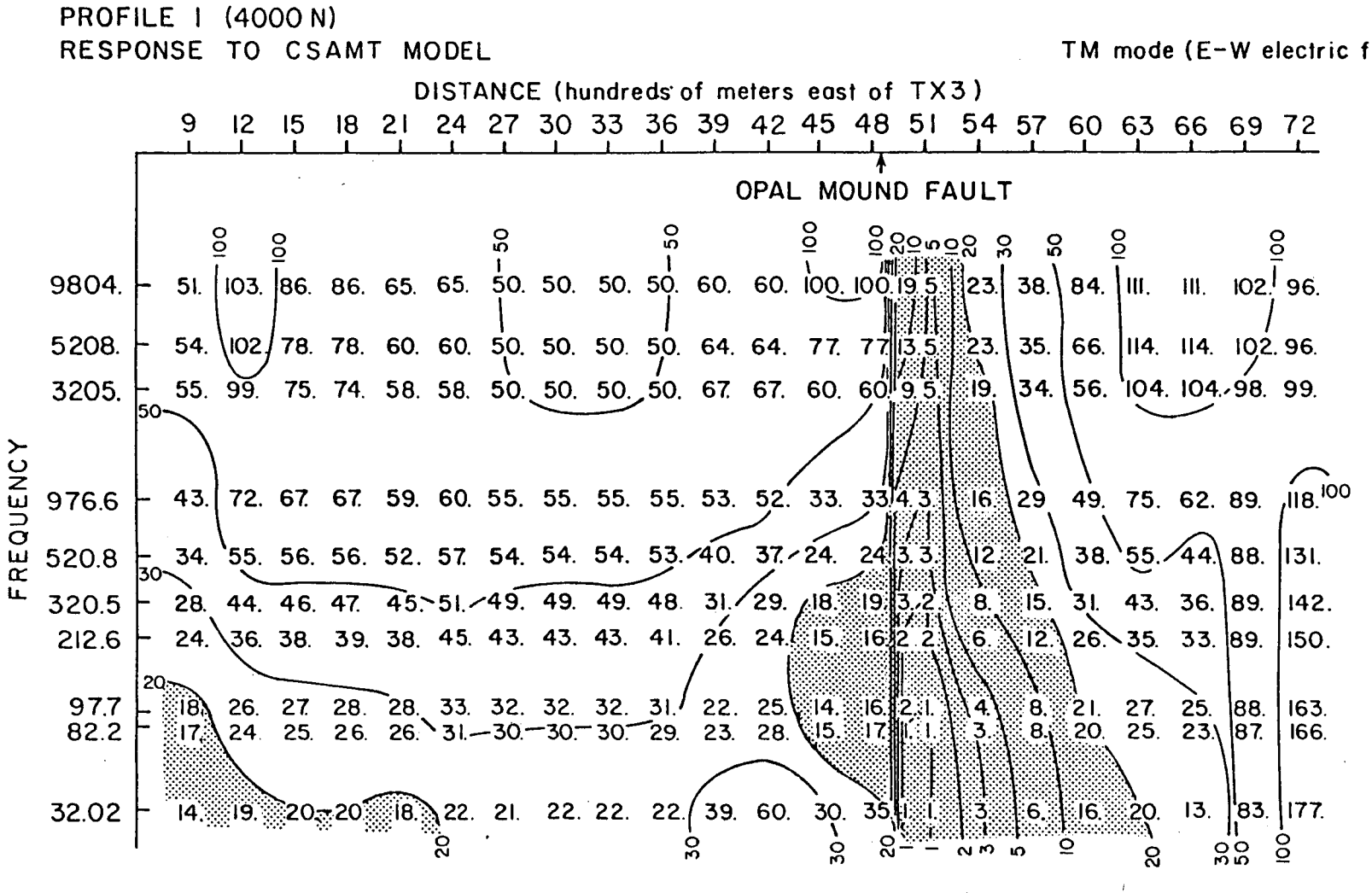

Figure 16. Theoretical TM mode pseudosection calculated from 2D CSAMT model of Profile One (4000 N). Apparent resistivity less than 20 ohm-m is shaded. Compare with field data in Figure 13.

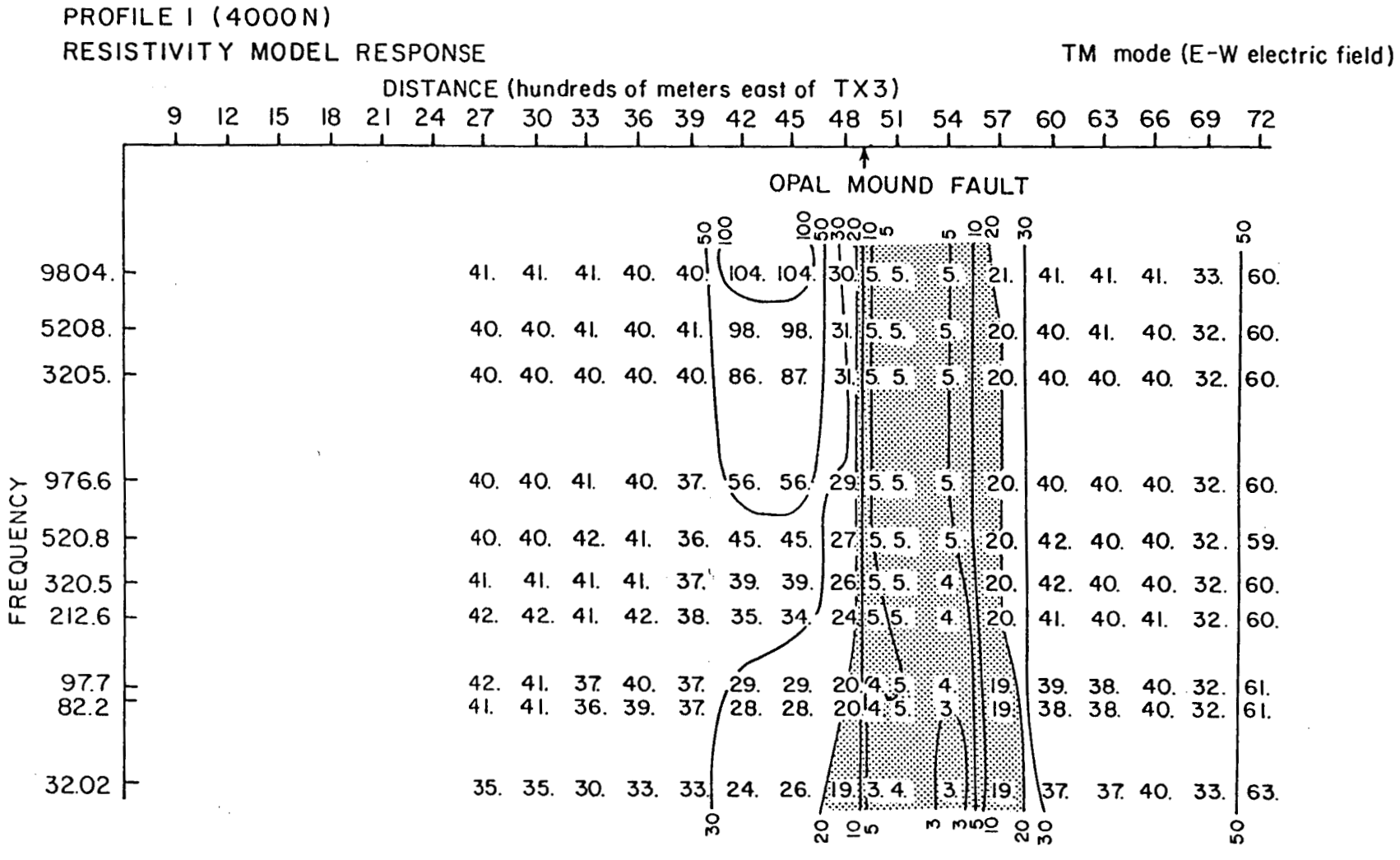

Figure 17. Theoretical TM mode pseudosection calculated from 2D dipole-dipole resistivity model of Profile One (4000 N). Apparent resistivity less than 20 ohm-m is shaded. Compare with field data in Figure 13.

One large disagreement between the resistivity and CSAMT interpretations is the depth to the conductive unit from stations 2400 to 3600 (Figure 15). This depth is modeled 300 m deep by resistivity, and 150 m deep by CSAMT. Joint modeling of 300 m and 1 km dipole-dipole data by Ward and Sill (1976) on this line also indicates a resistive-to-conductive interface at 300 m. The similarity between TM and TE mode CSAMT data in this region (see Figures 13 and 14) suggests that one-dimensional inversion results should be meaningful. We inverted data from stations 2400 through 3600 to determine the depth to this conductive zone. The resulting inversions are summarized in Table 2.

Inversion results indicate that the 150-m interface modeled by CSAMT is a shallow limit, and the 300 m interface modeled by resistivity is too deep. An inversion of Schlumberger resistivity sounding data (Tripp, 1977) obtained just west of station 3300 indicates a resistive-to-conductive interface at about 119 m with a range of 73 to 196 m. When EM sounding data (10.5 Hz to 86 KHz) in the same position were inverted (Tripp, 1977) 15 m of 119 ohm-m overburden underlain by 55 ohm-m material was interpreted. The EM sounding, although unable to penetrate to the resistive-conductive interface, gave a check on the resistivity of the upper layer. Based on this information, the upper layer resistivity for the CSAMT inversion was constrained at 50 ohm-m, eliminating high parameter correlations.

A 300 ohm-m resistive body corresponding to bedrock at depth is the main feature in the CSAMT section from 3900 to 4800. This body

Table 2. One-dimensional inversion results for stations 2400, 2700, 3000, 3300, and 3600 using TM mode field data. The data fit error, e, is calculated from s, the average squared error by the formula: $e = (\exp[s^{1/2}]-1)\cdot 100$.

Station	ρ_1	ρ_2	ρ_3	t_1	t_2	data fit error
2400	20,408. (6.9×10^5%)	51 (24%)	8.9 (61%)	7.7 (1778%)	141 (98%)	2.08×10^{-2} (16%)

Correlation Matrix

	ρ_1	ρ_2	ρ_3	t_1	t_2
ρ_1	1				
ρ_2	-.02	1			
ρ_3	-.03	.42	1		
t_1	.99	.02	-.01	1	
t_2	-.97	.16	.24	-.96	1

Station	ρ_1	ρ_2	t_1	data fit error
2700	59 (15%)	9.9 (117%)	179 (39%)	8.53×10^{-2} (34%)
3000	45 (5.4%)	3.6 (104%)	237 (13%)	1.23×10^{-2} (12%)
3300	44.4 (11%)	.47 (556%)	257 (19%)	5.45×10^{-2} (26%)
3600	47 (10%)	8.7 (70%)	173 (24%)	2.21×10^{-2} (16%)

Correlation Matrices

Station 3300

	ρ_1	ρ_2	t_1
ρ_1	1.0		
ρ_2	.31	1.0	
t_1	.26	.78	1.0

Station 3600

	ρ_1	ρ_2	t_1
ρ_1	1.0		
ρ_2	.34	1.0	
t_1	.49	.83	1.0

Station 2700

	ρ_1	ρ_2	t_1
ρ_1	1.0		
ρ_2	.29	1.0	
t_1	.42	.82	1.0

Station 3000

	ρ_1	ρ_2	t_1
ρ_1	1.0		
ρ_2	.30	1.0	
t_1	.33	.81	1.0

is modeled 150 m deep, but the depth is not well resolved. It is not shown in the interpretation of the dipole-dipole data (Figure 15b). The evidence for this resistive block occurs at the two lowest frequencies at stations 4200, and 4500, and the lowest frequency at stations 3900, and 4800. Two-dimensional Schlumberger modeling 500 m to the south of this line (Tripp, 1977) delineates a 300 ohm-m block at a similar depth. The joint 300 m and 1 km dipole-dipole model (Ward and Sill, 1976) indicates a 300 ohm-m substratum 600 m deep from station 3900 eastward.

The ability to resolve a narrow resistive structure at depth is related to the depth of exploration. The CSAMT technique, using the skin depth criterion, has a depth of exploration in 10 ohm-m material of 280 m (at 32 Hz). However, sensitivity tests indicate that the depth of exploration is less than a skin depth with our instrumentation due to apparent resistivities being repeatable only within a factor of 1.26. The dipole-dipole technique at n = 4 has depths of exploration of about 120 m, 360 m, and 1200 m for 100 m, 300 m, and 1 km dipoles respectively (Roy and Apparao, 1971) for a plane interface. For tabular vertical structures, depths of exploration are less than for a plane interface. However, the 300 m dipole-dipole data should include information about the 300 ohm-m block, but likely due to non-uniqueness of resistivity modeling, this block was not modeled (see Figure 15b).

Gravity modeling on this line (Crebs, 1976) shows bedrock 70 m deep below station 4800 increasing to about 140 m just west of station 4200. By adjusting the density contrast to a more reasonable

value, Tripp (1977) suggested that the depth could compare quite reasonably with the 150 m modeled here. This resistive body is most likely unaltered precambrian gneiss bedrock.

A thermal gradient hole was drilled a short distance from station 4800, intersecting the water table at 35 m. This distance coincides with the CSAMT model interface between 100 ohm-m and 10 ohm-m material at 40 m depth.

Just east of station 4800 there is a sharp surface lateral resistivity contrast corresponding to the Opal Mound fault mapped by resistivity, heat flow, and geology. Inversion of EM sounding data shows 19 m of 24 ohm-m material underlain by 3.4 ohm-m material in this position (Tripp, 1977). This agrees well with the CSAMT model of 15 m of 30 ohm-m material underlain by 1 ohm-m material. The bottom of the 1 ohm-m block and the east edge of the 300 ohm-m block (see Figure 15), are not resolved because the near surface region is so conductive that it is impossible to "see through" it at these frequencies. The eastern end of the 1 ohm-m unit is modeled as a staircase structure which implies a shallow, eastward dipping altered zone east of the Opal Mound fault.

A sensitivity study helped to explain the lack of fit in the theoretical dipole-dipole pseudosection (Figure 18) from station 5100 eastward. An AMT one-dimensional study to simulate the resistivity section beneath station 5100 indicated that it was not possible to determine the resistivity of anything below a 15 m layer of 5 ohm-m material overlying 60 m of 1 ohm-m material, even though a skin depth in 1 ohm-m material at 32 Hz is 89 m. When the errors in data

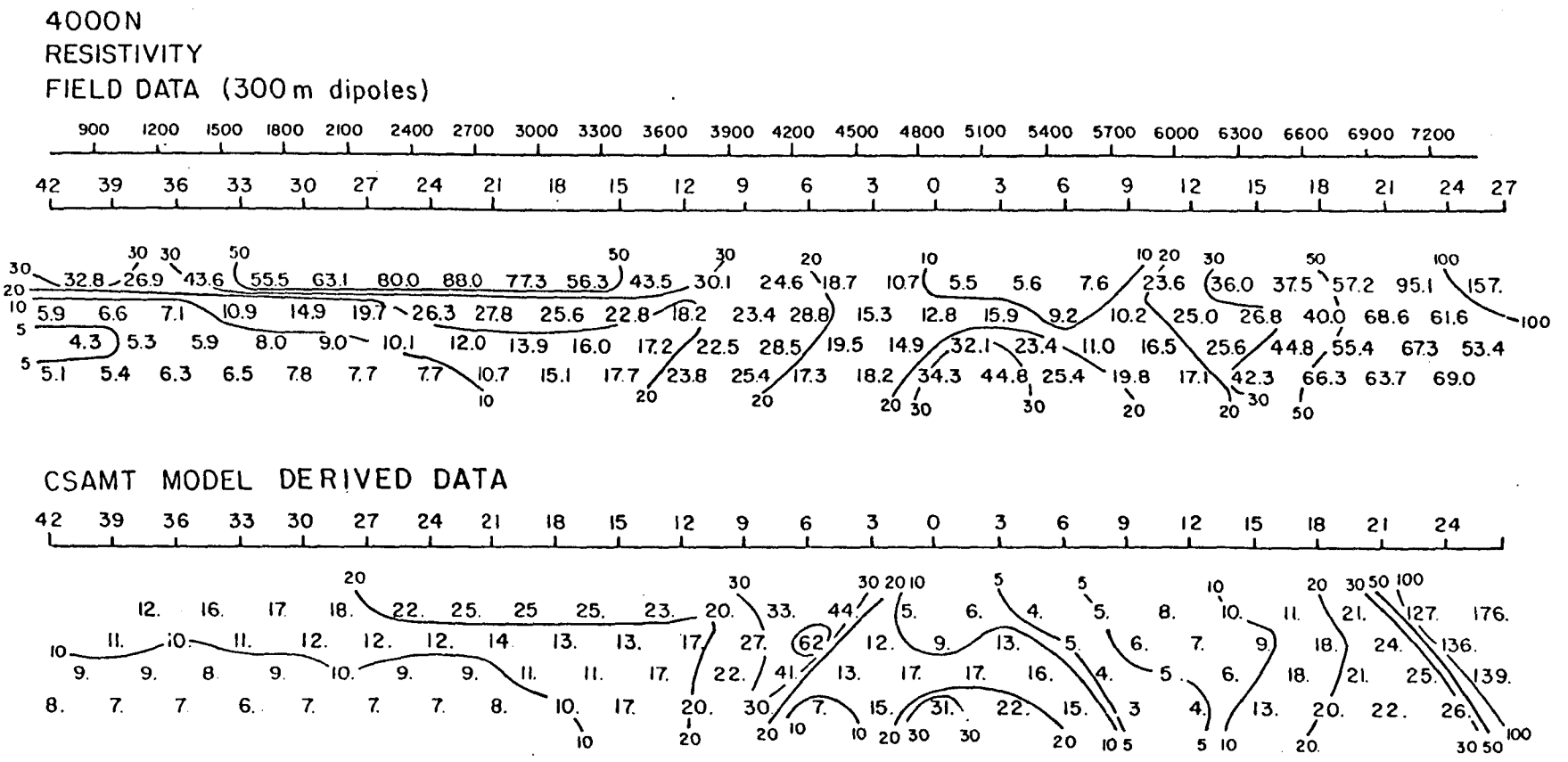

Figure 18. Dipole-dipole (a = 300 m) resistivity field data compared with theoretical dipole-dipole data calculated from the CSAMT model of Profile One (4000 N).

measurement are considered, the thickness of the 1 ohm-m layer could be decreased to about 40 m and still shield information from below. Therefore, the exploration depth in this case is less than .6 skin depths.

A similar study simulating the resistivity section beneath station 5400 indicated that no information could be derived about material below a 20 ohm-m layer 30 m thick overlying a 1 ohm-m layer 45 m thick. The depth of exploration is therefore less than .8 skin depths.

Based upon the sensitivity tests, a model similar to the CSAMT model in Figure 15 was constructed which fit the 300 m dipole-dipole data out to station 6000. The modified model included thinning the 1 ohm-m layer and inserting 40 ohm-m material beneath it under stations 5100 to 5700. Lack of fit east of station 6000 is likely due to the fact that the area is not two-dimensional because of faulting parallel to the traverse 500 m to the north (Nielson et al., 1978).

Profile Two

Profile Two is an east-west traverse along resistivity line 2200N, and is located 1800 meters south of Profile One (see Figure 9). The data are plotted in pseudosection form in Figure 19. Five stations in the center of the line (6W, 3W, 0, 3E, and 6E) were obtained using transmitter TX4, and the rest were taken by working off both ends of transmitter TX5 (an E-W, 2000 ft (609.6 m) bipole). Hence the data shown in Figure 19 are for the TM mode (i.e., E-W electric field).

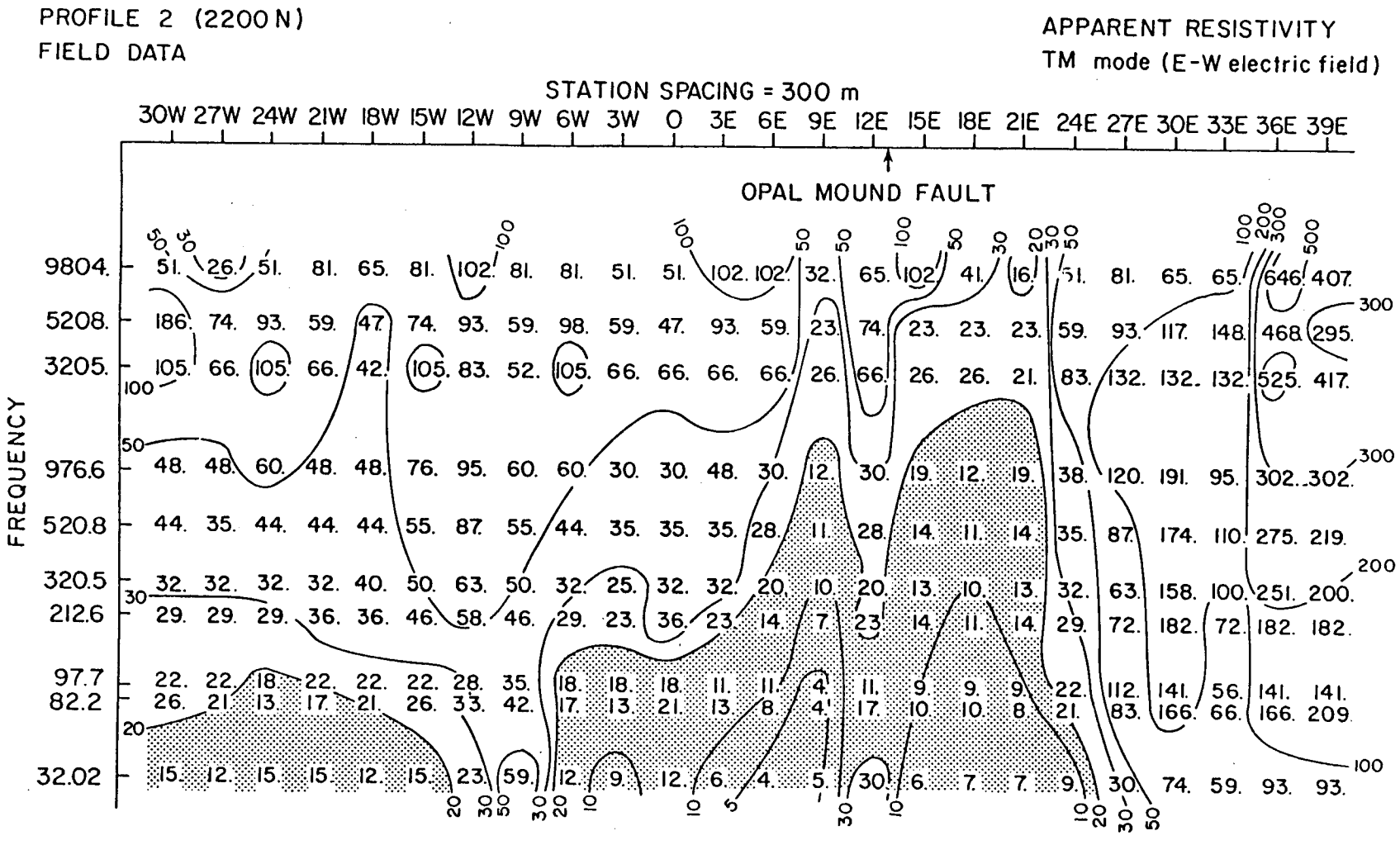

Figure 19. Field data pseudosection from Profile Two (2200 N). Apparent resistivity less than 20 ohm-m is shaded.

Low-frequency data at station 9W erroneously indicate a resistive body at depth, because the station was too close to the transmitter. For a 50 ohm-m earth at 32 Hz, the distance from the center of the transmitter (at 0) to 9W is only 1.4 skin depths. Thus the low-frequency data at station 9W were not modeled.

As in the previous profile, one-dimensional MT inversion was used at individual stations to construct an initial two-dimensional model. Iterative two-dimensional forward MT modeling improved the data fit, resulting in the CSAMT interpretation model in Figure 20a. The data fit is illustrated by comparing the theoretical data in Figure 21 with the field data in Figure 19. Figure 20b shows a two-dimensional dipole-dipole resistivity model of the same line (Ross et al., 1980) for comparison. Again, a theoretical AMT pseudosection derived from the resistivity model (not shown) does not fit the field data very well.

The resistivity and CSAMT models are somewhat similar. At 6W on the profile, the resistive-to-conductive interface depth is 90m in the resistivity model compared to 70 m in the CSAMT model, although the resistivity values are different.

A gravity interpretation of this profile (Crebs, 1976) shows a 230 m wide bedrock horst below station 12E buried 30 m deep. The Opal Mound fault lies on the east flank of this horst. We modeled a resistive block 300 m wide, 155 m from the surface in the same position. A value of 300 ohm-m was chosen for the resistivity to coincide with a similar bedrock structure on Profile One. The model derived from dipole-dipole resistivity data indicates a similar

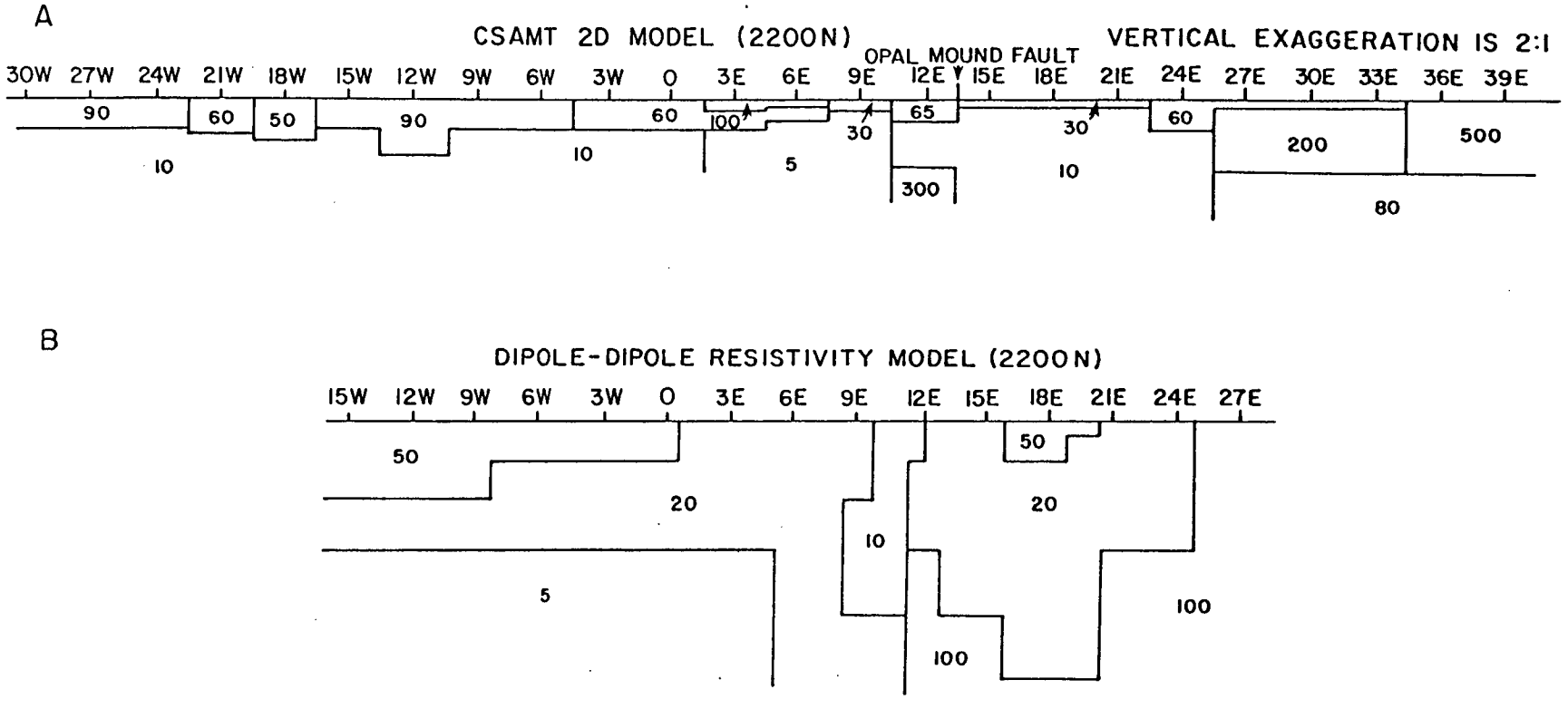

Figure 20. (a) Two-dimensional CSAMT and (b) dipole-dipole resistivity (based on 100 m and 300 m dipoles) interpretations of Profile Two (2200 N).

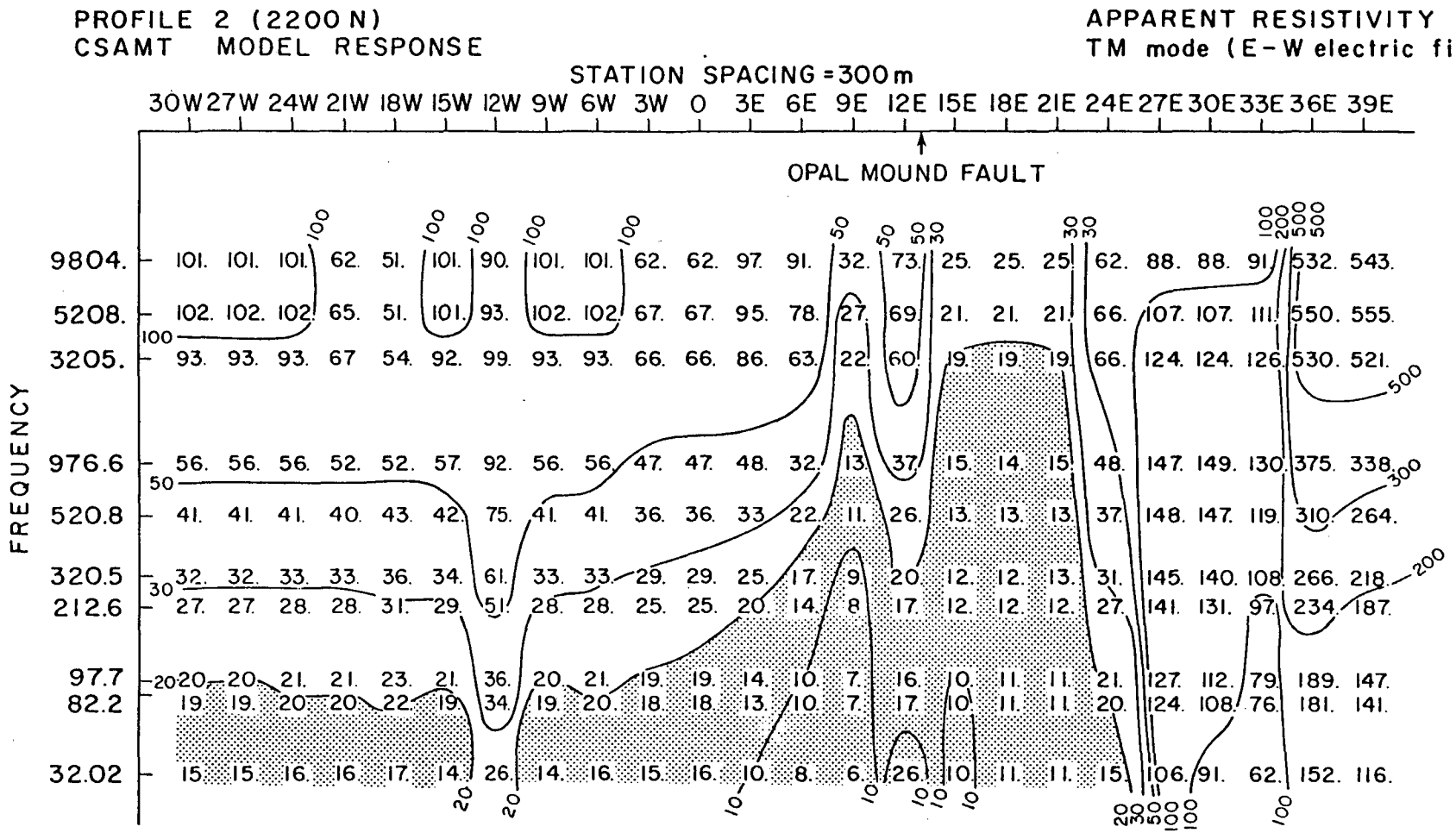

Figure 21. Theoretical pseudosection calculated from 2D CSAMT interpretation of Profile Two (2200 N). Apparent resistivity less than 20 ohm-m is shaded. Compare with field data in Figure 19.

resistive structure at station 1200E: a 100 ohm-m block 150m wide and 300m deep. This resistive structure, an extension of the one from profile one, is most likely unaltered precambrian gneiss bedrock.

Another similarity between the CSAMT and resistivity models is a contact between 24E and 27E. Resistivity increases to the east corresponding to the unaltered but weathered granitic Mineral Mountains pluton.

CONCLUSIONS

Controlled source AMT appears to be an effective method for rapidly mapping the near-surface expression of a geothermal system. CSAMT resistivity mapping at Roosevelt Hot Springs KGRA delineates the same low-resistivity zones as those shown on a first separation 300-m dipole-dipole resistivity map. However, the CSAMT data were collected more rapidly because stations were not constrained to lines, long wires were not necessary, and only two transmitter sites were required. While no cost study was made, we believe that CSAMT would be cost comparable, or more likely, more cost effective than dipole-dipole resistivity mapping in a geothermal environment.

Profiling with CSAMT using 10 frequencies and subsequent 2D TM modeling produced interpretations consistent with other geoscience evidence. Two-dimensional modeling of Profile One, supported by gravity data, indicates a resistive structure at depth likely corresponding to unaltered bedrock beneath stations 3900 to 4800. A shallow, eastward-dipping conductive zone, probably altered alluvium due to brine leakage from the Opal Mound fault, is indicated from stations 5100 to 5700. Profile Two indicates a resistive structure at depth below station 12E in the same position as a bedrock horst modeled by gravity. Alteration and/or brine leakage is indicated on both east and west sides of the Opal Mound fault along Profile Two.

A good initial guess for a 2D CSAMT model can be obtained by

stitching together 1D inversions for all stations, since lateral effects are small at AMT frequencies. This appears to be an advantage over dipole-dipole 2D modeling where an initial guess is not as easily obtained.

The ambiguity of electrode effects inherent in the dipole-dipole technique are not present in CSAMT since the receiver samples only the ground nearby which is independent of the transmitter. Since the transmitter is far enough removed, the source field is approximately a plane wave yielding measurements which are source independent.

Skin depth considerations suggest that CSAMT mapped the electrical resistivity to 300 m depth in conductive areas. However, modeling and sensitivity tests confirmed the findings of Strangway et al. (1973) that the technique has difficulty detecting structure beneath conductive overburden. Depth of exploration, given the accuracy of our measurements, was found to be considerably less than a skin depth in conductive areas.

APPENDIX A

CATALOG OF TWO-DIMENSIONAL AMT MODELS

A catalog of two-dimensional (2D) AMT models was assembled in order to provide an interpretation guide when computer modeling is not available. Models are apparent resistivity pseudosections computed at four frequencies: 10, 100, 1000, and 10000 Hz. Two pseudosections are given for each model: TM (E-perpendicular to strike), and TE (E-parallel to strike).

The TM mode is more useful in practice, because real 2D electrical structures seldom occur in the field (Wannamaker, 1980). Charge accumulations at discontinuities along strike prevent a true TE response. The TM response of a 3D body with a relatively short strike length is more accurately represented by 2D modeling than the TE response. Because of this, TM pseudosections are emphasized in the following comments on each model.

1. Vertical Contact - Figure A1

In the TM mode, an "overshoot" in apparent resistivity occurs on the resistive side, and a resistivity "undershoot" occurs on the conductive side. At low frequencies background resistivities are not reached even 320 meters away laterally.

2. Buried Contact - Figure A2

The resistivities at the highest frequency on the right side in

both modes are greater than the overburden resistivity (100 Ω-m). In the TM mode, apparent resistivities at the two lowest frequencies on the left side "overshoot" the background resistivity (100 Ω-m).

3. Small Conductive Surface Body - Figure A3

Resistivity contours define the lateral position of the body well in the TM mode. Resistivities at the three lowest frequencies over the center of the body in the TM mode are constant, indicating the body has small depth extent. The TE mode pseudosection also shows that the body has a small depth extent.

4. Buried Conductive Body With Large Depth Extent (Contrast 10) - Figure A4

Resistivities over the body in the TM mode decrease with decreasing frequency indicating large depth extent. Response is similar to that of a buried contact on each side. Resistivities over the center of the body in the TE mode start to increase at 10 Hz, indicating that the background resistivity is starting to affect the apparent resistivity. Compare with A8.

5. Buried Conductive Body With Large Depth Extent (Contrast 20) - Figure A5

Figures A4 and A5 are similar in the TM mode indicating that this more conductive body is indistinguishable from the previous one. The TE mode apparent resistivities in the two figures are much different at 100 and 10 Hz indicating that the models were different.

6. Outcropping Body With Large Depth Extent - Figure A6

Resistivities in the center of the TM pseudosection decrease with decreasing frequency indicating large depth extent. Contours define the lateral position of the body well in the TM mode. Compare with A7.

7. Outcropping Slab - Figure A7

Resistivities in the center of the TM pseudosection remain constant with decreasing frequency indicating shallow depth extent. TM contours define the lateral position well. Compare with A6.

8. Buried Slab - Figure A8

Resistivities in the center of the TM pseudosection do not decrease as fast with decreasing frequency as in figure A4, indicating small depth extent. Compare with A4 and A7 to see effects of depth extent and burial, respectively.

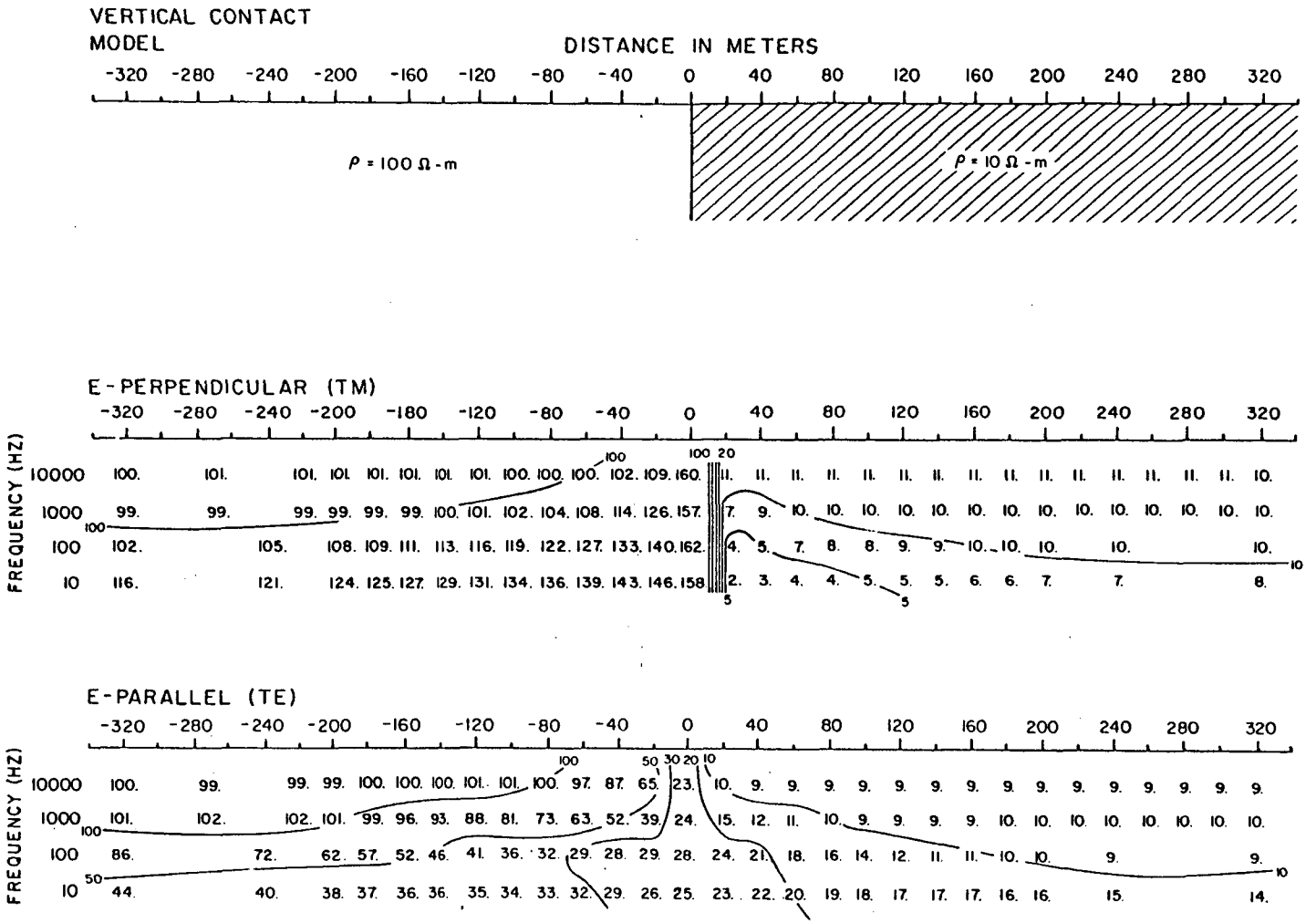

Figure A1. Vertical contact AMT model and pseudosections for transverse magnetic (TM) and transverse electric (TE) configurations.

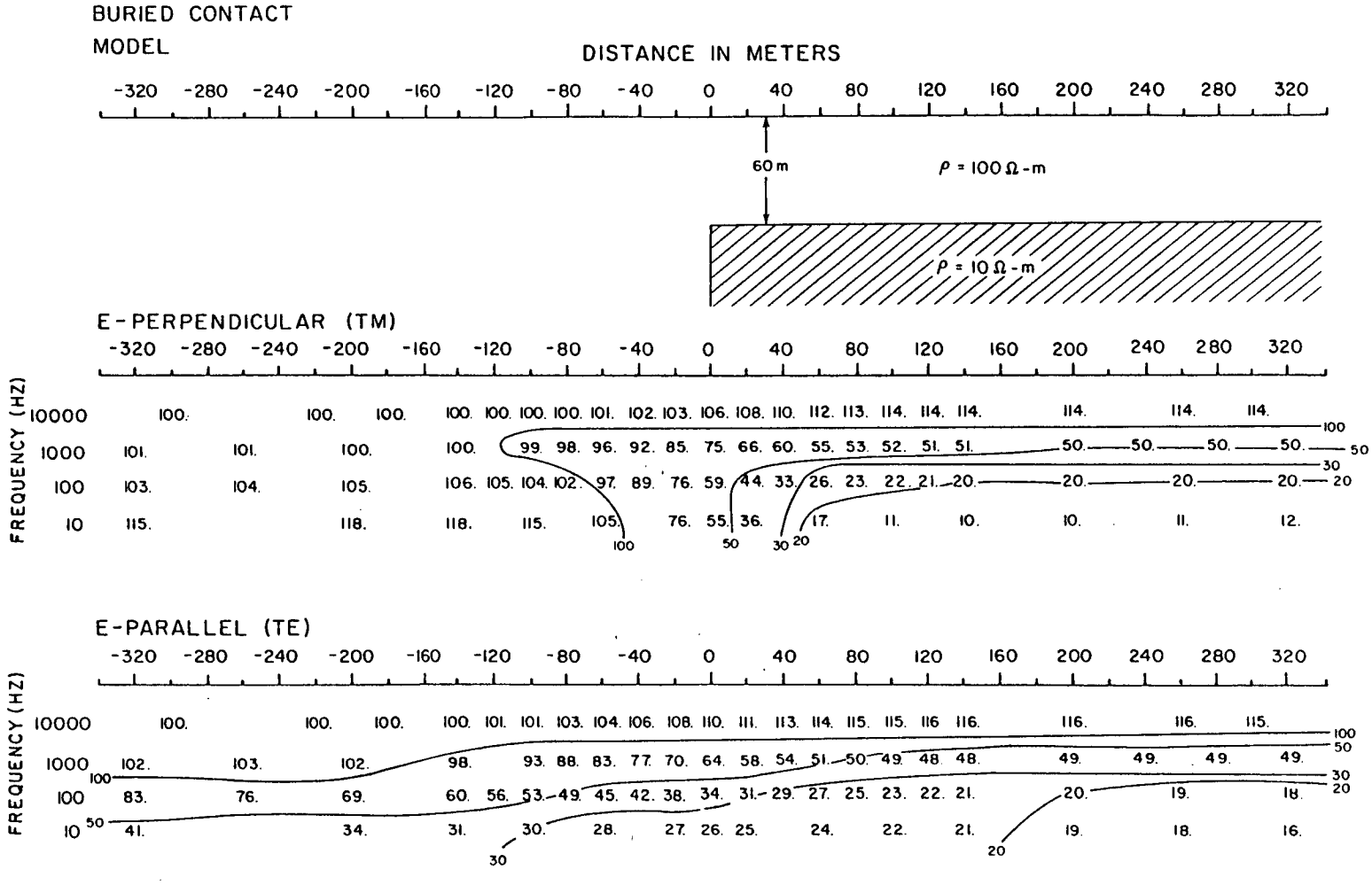

Figure A2. AMT model for a buried contact and resulting pseudosections.

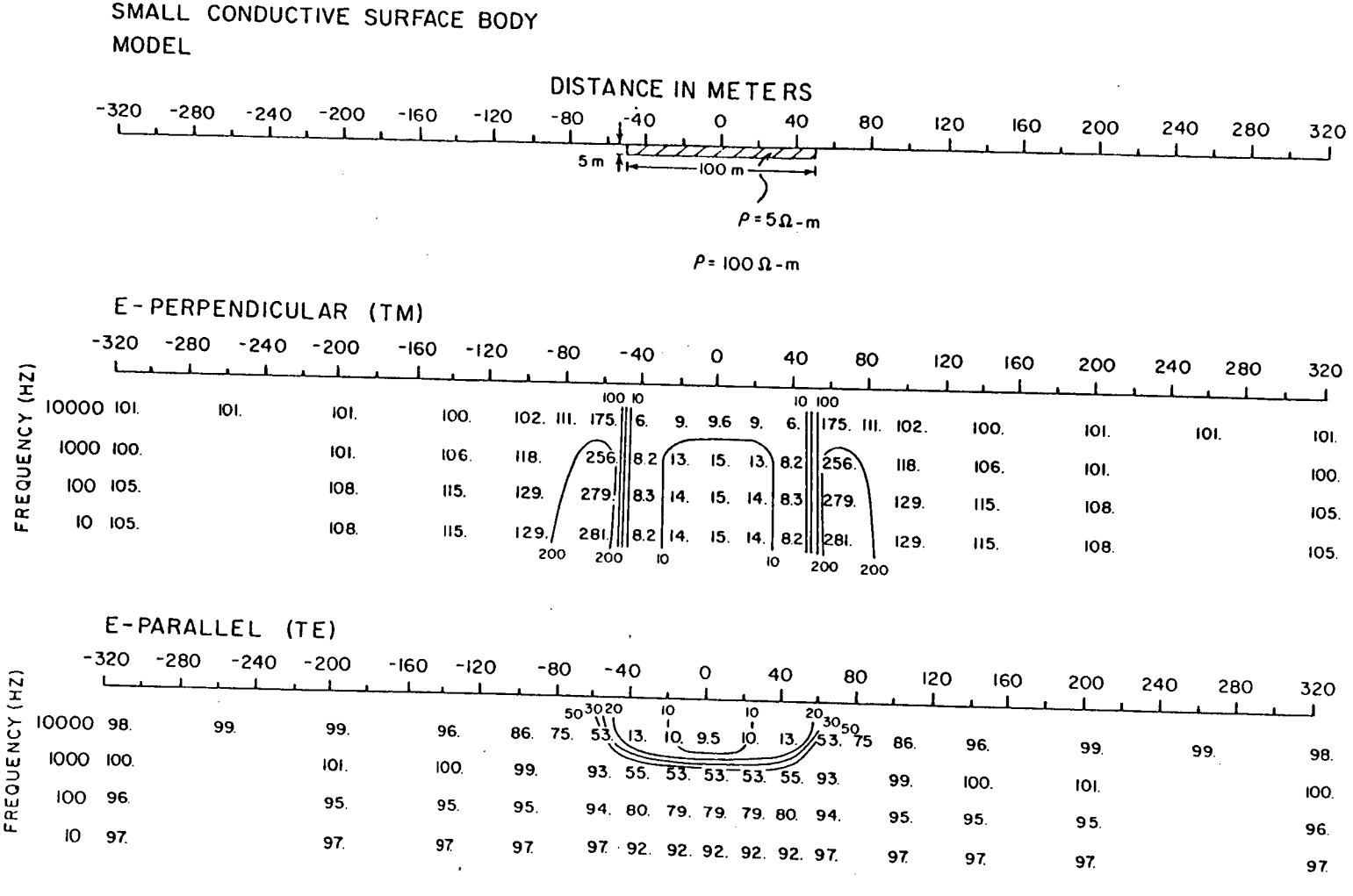

Figure A3. AMT model for a small, near-surface, conductive body and resulting pseudosections.

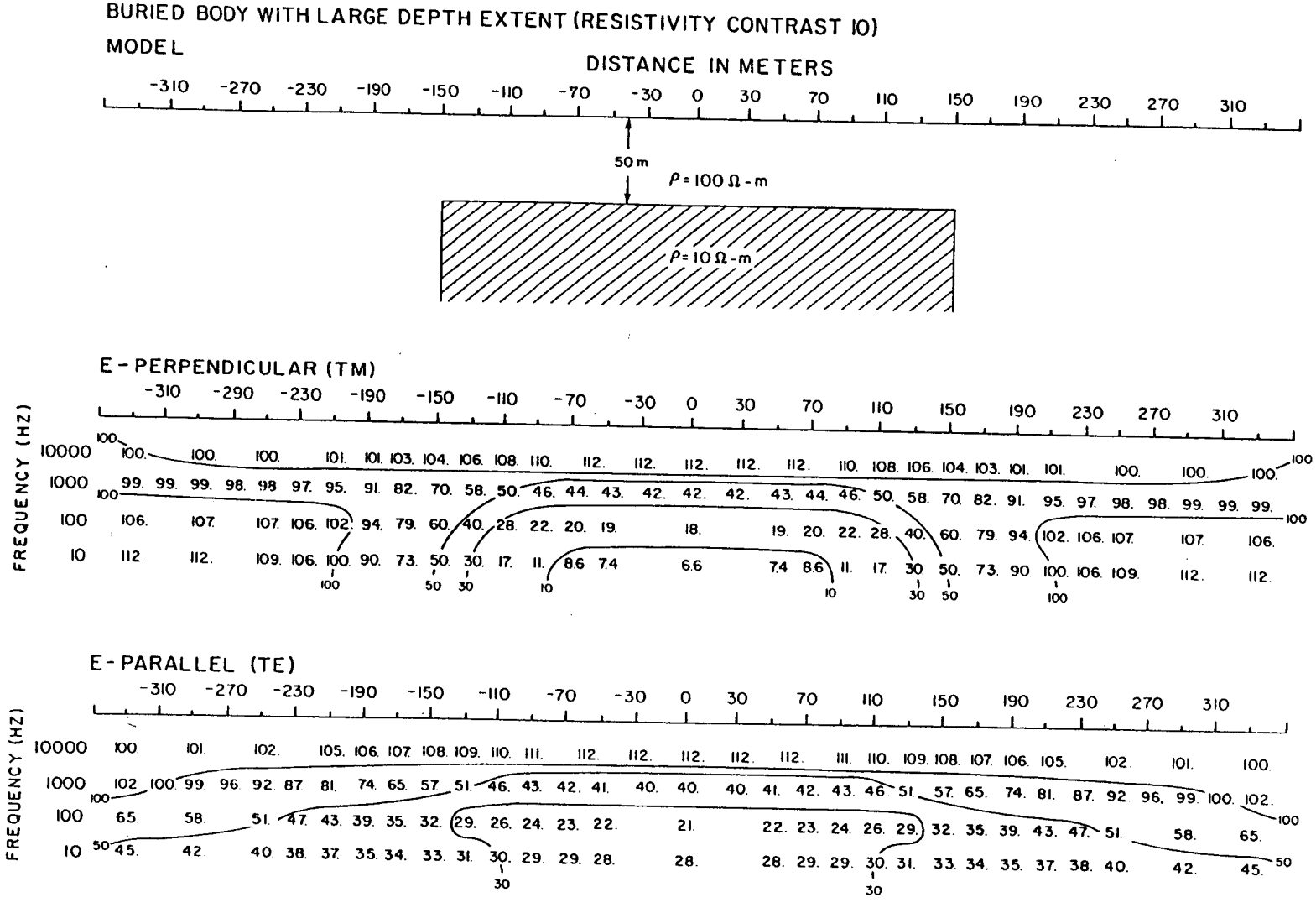

Figure A4. AMT model for a buried, conductive body of large depth extent and resulting pseudosections. Resistivity contrast of 10.

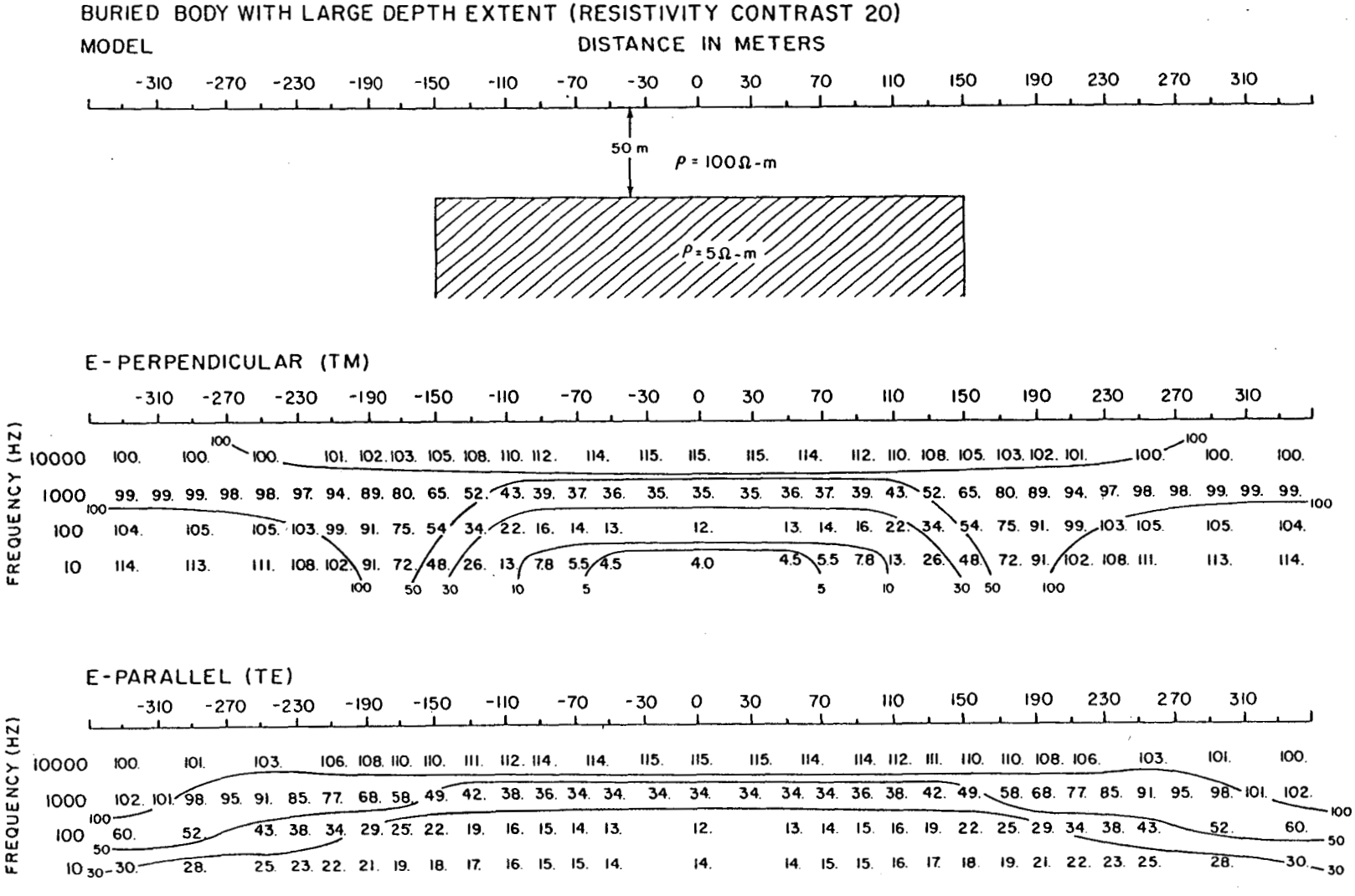

Figure A5. AMT model for a buried, conductive body of large depth extent and resulting pseudosections. Resistivity contrast of 20.

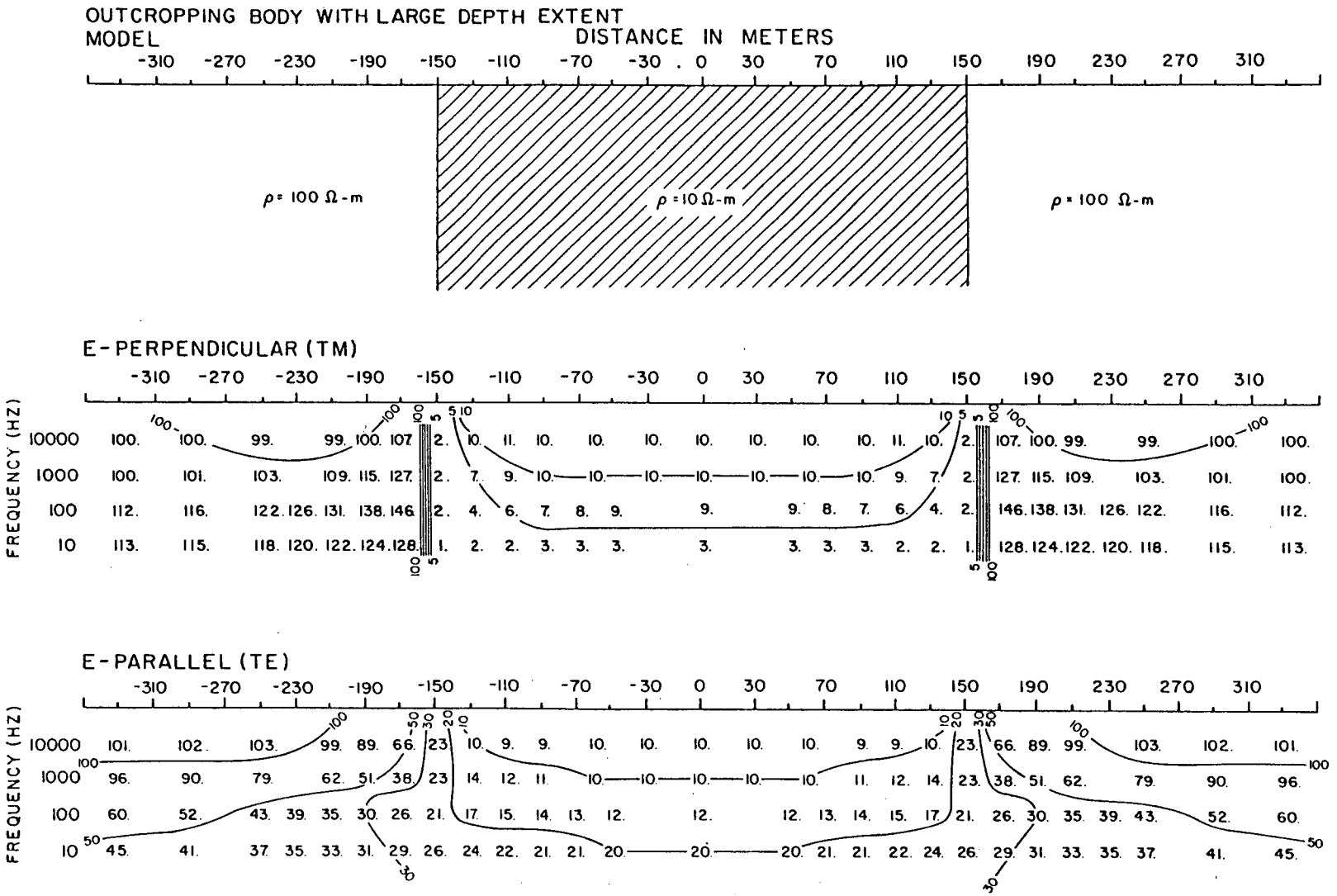

Figure A6. AMT model for a body of large depth extent exposed at the surface and the resulting pseudosections.

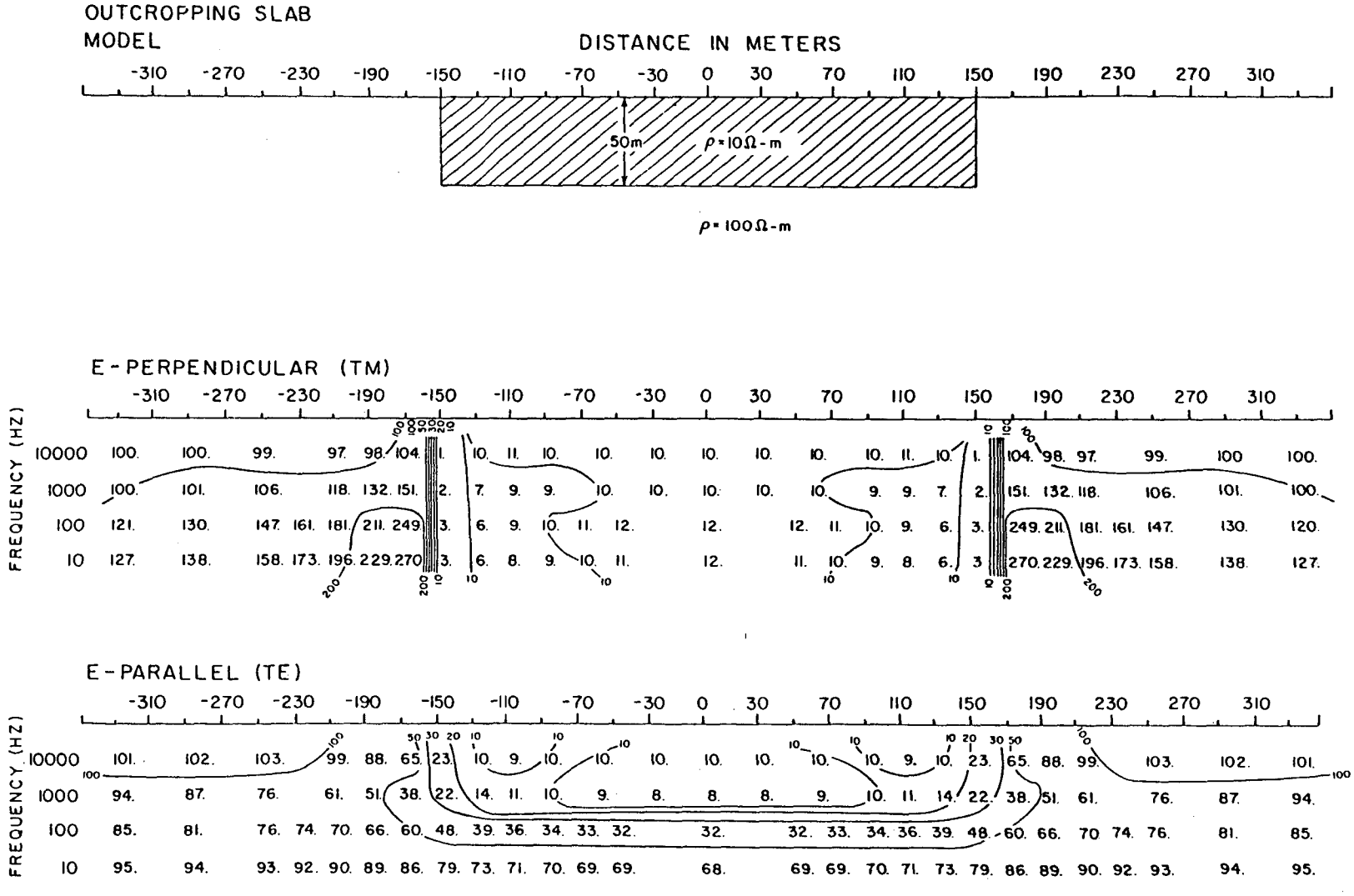

Figure A7. AMT model and resulting pseudosections for a slab exposed at the surface.

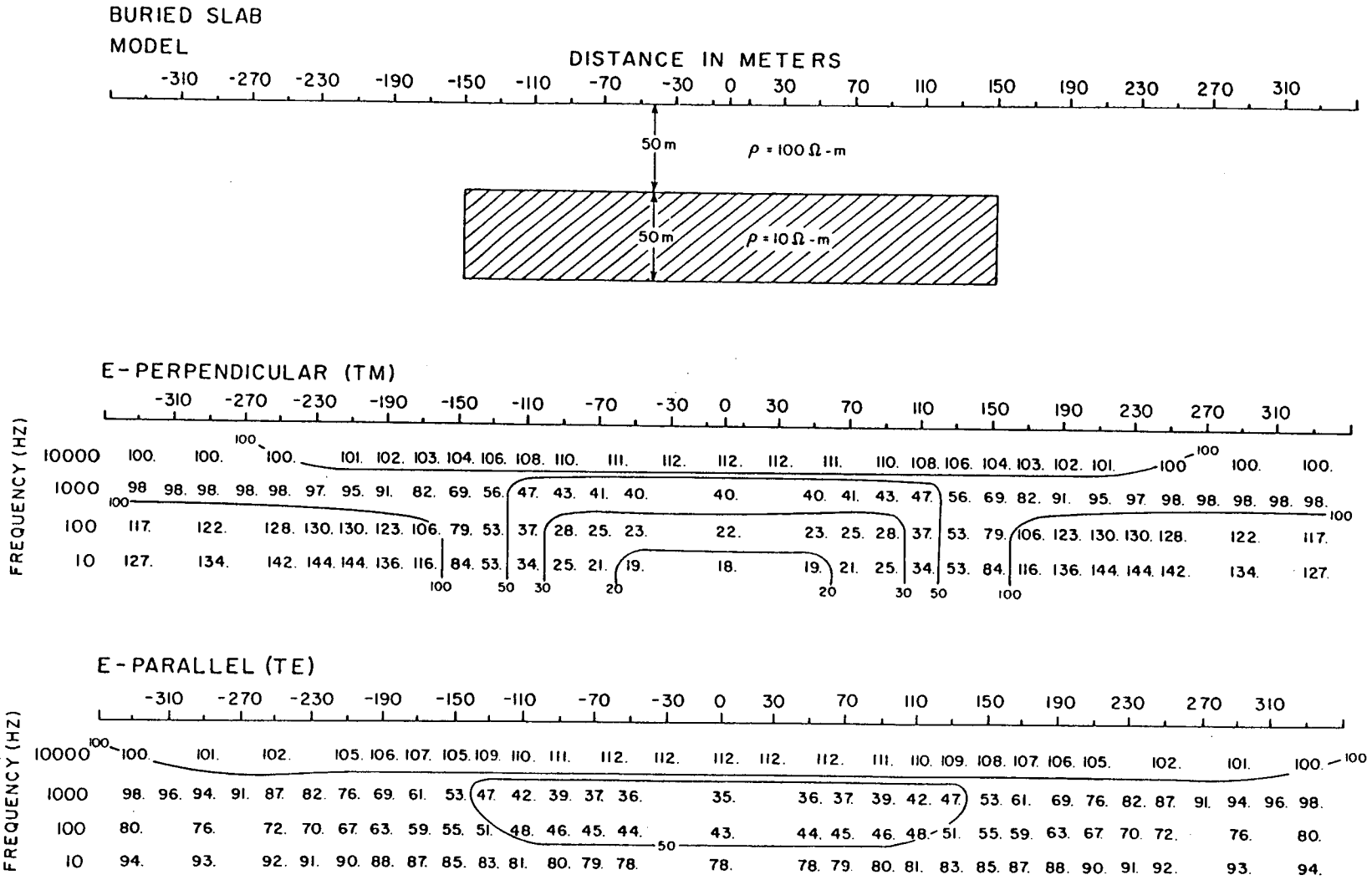

Figure A8. AMT model and resulting pseudosections for a buried slab.

APPENDIX B

VALIDITY OF THE PLANE WAVE APPROXIMATION

The equations we used for the horizontal components of the fields over a half-space due to an infinitesimal electric dipole in the x-direction are:

$$E_x = \frac{I\ell(x^2-y^2)}{2\pi r^3 \hat{y}} \int_0^\infty \lambda e^{-u_1 z'} J_1(\lambda r)\, d\lambda - \frac{I\ell}{2\pi r^3 \hat{y}} \int_0^\infty \frac{x^2\lambda(\lambda+u_1) - r_1 k_1^2}{u_1+\lambda} e^{-u_1 z'} \lambda J_0(\lambda r)\, d\lambda$$

$$E_y = \frac{I\ell xy}{\pi r^3 \hat{y}} \int_0^\infty e^{-u_1 z'} \lambda J_1(\lambda r)\, d\lambda - \frac{xyI\ell}{2\pi r^2 \hat{y}} \int_0^\infty e^{-u_1 z'} \lambda^2 J_0(\lambda r)\, d\lambda$$

$$H_x = -\frac{I\ell xy}{\pi r^3} \int_0^\infty \frac{\lambda e^{-u_1 z'}}{u_1+\lambda} J_1(\lambda r)\, d\lambda + \frac{I\ell xy}{2\pi r^2} \int_0^\infty \frac{\lambda^2 e^{-u_1 z'}}{u_1+\lambda} J_0(\lambda r)\, d\lambda$$

$$H_y = \frac{I\ell}{2\pi r} \int_0^\infty \left\{ \frac{1}{r^2}\left[y^2\left(\frac{u_1-\lambda}{u_1+\lambda}\right) + x^2\right] - \frac{u_1}{u_1+\lambda} \right\} e^{-u_1 z'} J_1(\lambda r)\, d\lambda - \frac{I\ell}{4\pi r^2} \int_0^\infty \left[y^2\left(\frac{u_1-\lambda}{u_1+\lambda}\right) + x^2\right] e^{-u_1 z'} \lambda J_0(\lambda r)\, d\lambda$$
$$+ \frac{I\ell}{4\pi} z'(r^2+z'^2)^{-3/2}\left[1 + ik_1(r^2+z'^2)^{1/2}\right] e^{-ik_1(r^2+z'^2)^{1/2}}$$

These equations are so complicated that they cannot be analyzed easily. Goldstein and Strangway (1975) tested the half-space solutions numerically to determine the validity of the plane wave approximation. However, the fields in a whole space are easier to understand and by analogy they can be used to analyze the half-space field behavior.

The fields at a distance r from a z-oriented electric dipole in a conductive whole space are (Harrington, 1961 p. 79):

$$E_r = \frac{I\ell}{2\pi} e^{-ikr}\left(\frac{\eta}{r^2} + \frac{1}{\hat{y} r^3}\right)\cos\theta$$

$$E_\theta = \frac{I\ell}{4\pi} e^{-ikr}\left(\frac{\hat{z}}{r} + \frac{\eta}{r^2} + \frac{1}{\hat{y}r^3}\right)\sin\theta$$

$$H_\phi = \frac{I\ell}{4\pi} e^{-ikr}\left(\frac{ik}{r} + \frac{1}{r^2}\right)\sin\theta$$

where I = current, ℓ = dipole length, $k = -\sqrt{\hat{z}\hat{y}}$, $\eta = \sqrt{\frac{\hat{z}}{\hat{y}}}$.

The magnetic field is linearly polarized, but the electric field is elliptically polarized since it has two components. The near-source terms (the $1/r^2$ and $1/r^3$ terms) are dominant close to the current element. At large distances the $1/r$ term in E_θ dominates and the electric field becomes linearly polarized. Harrington (1961, p. 79) states that in the far-field these fields reduce to

$$E_\theta = \eta \frac{iI\ell}{2\lambda r} e^{-ikr}\sin\theta$$

$$H_\phi = \frac{iI\ell}{2\lambda r} e^{-ikr}\sin\theta \quad , \quad r \gg \lambda = \frac{2\pi}{k}$$

When these are substituted in the formula for scalar apparent resistivity, we obtain

$$\rho_a = \frac{1}{\mu\omega}\left(\frac{|E|}{|H|}\right)^2 = \frac{1}{\mu\omega}|\eta|^2 = \frac{1}{\mu\omega}\left|\frac{\hat{z}}{\hat{y}}\right| \cong \frac{\mu\omega}{\mu\omega\sigma} = \rho$$

We would like to know the distances at which the far-field term becomes equivalent to the near-field terms and where it is 10 times greater than the near field terms.

E_θ can be written in terms of skin depth $\delta = \sqrt{\frac{2}{\mu\omega\sigma}}$

$$E_\theta = \frac{I\ell}{4\pi} e^{-ikr}\frac{1}{\hat{y}}\left(\frac{2i\left(\frac{r}{\delta}\right)^2 + (1-i)\frac{r}{\delta} + 1}{r^3}\right)\sin\theta$$

The magnitudes of the $1/r$ term and the $1/r^2$ and $1/r^3$ terms become equivalent where

$$\left|2i\left(\frac{r}{\delta}\right)^2\right| = \left|(1-i)\frac{r}{\delta} + 1\right|$$

or $$2\left(\frac{r}{\delta}\right)^2 = \left[\left(\frac{r}{\delta} + 1\right)^2 + \frac{r}{\delta}\right]^{1/2}$$

which occurs when

$$\frac{r}{\delta} = 1.08$$

The far-field term is ten times greater than the near-field terms when

$$\left| 2i \left(\frac{r}{\delta}\right)^2 \right| = 10 \cdot \left| (1-i)\frac{r}{\delta} + 1 \right|$$

or

$$\frac{r}{\delta} = 6.15$$

The half-space fields by analogy should behave similarly. The ellipticity of the electric field approaches zero as the distance from the source increases, and the magnetic and electric fields become orthogonal.

In an analogous manner, the ellipticities of the horizontal components of the half-space fields approach zero as the distance from the source increases: The half-space fields become linearly polarized. The distance at which the far-field terms control the behavior should be indicated by the decrease in ellipticity.

For the finite source used, the angle between the major axes of the polarization ellipses of the electric and magnetic fields is plotted in Figure B1. Using the whole space as a guide, at large distances the angle should approach 90 degrees. In the far-field we assume that the fields become linearly polarized, with the electric and magnetic fields becoming orthogonal. Therefore, the far-field, where the plane wave approximation holds, is indicated by regions where the difference angle is close to 90 degrees. The region where

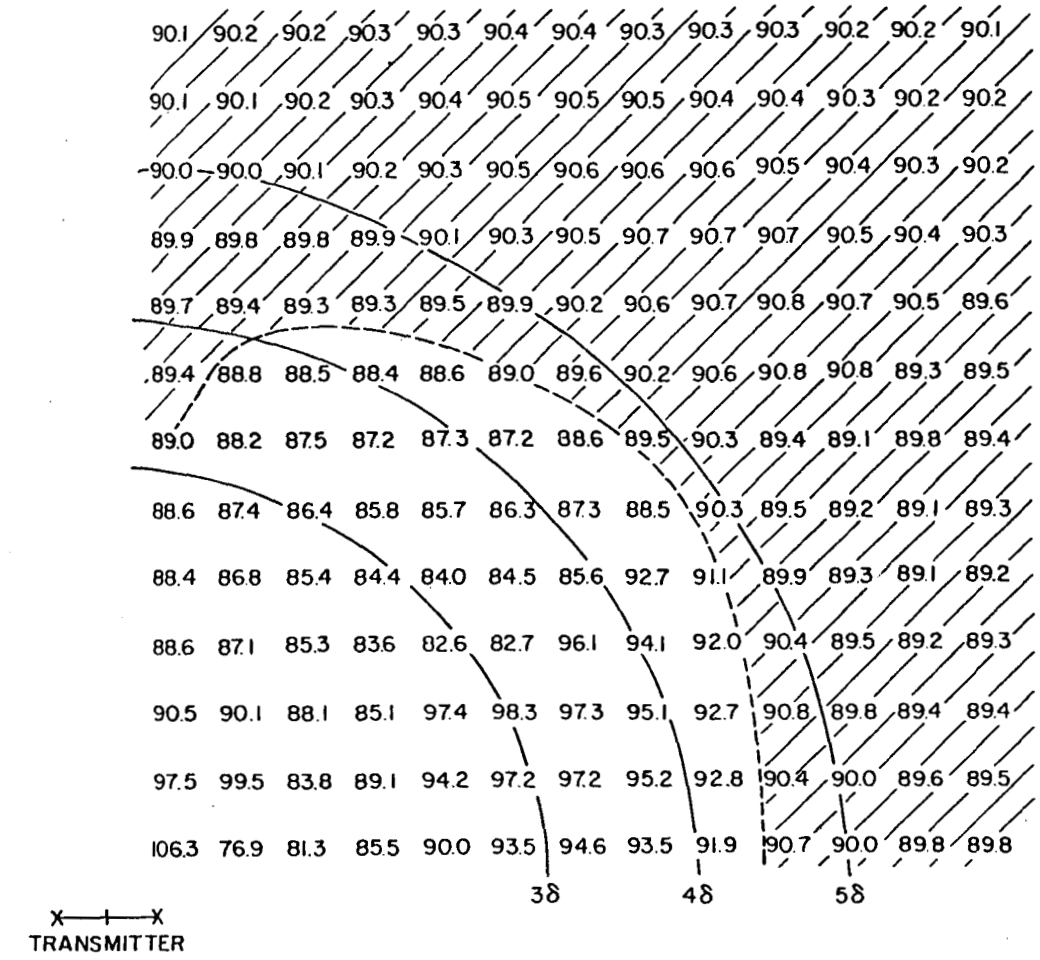

Figure B1. The angle between the major axes of the polarization ellipses of the electric and magnetic fields. Distances of 3, 4, and 5 skin depths (δ) from the center of the transmitter are shown. The shaded area is where the ellipse axes are within one degree of orthogonal.

difference angles are within one degree of orthogonal is shaded in Figure B1. Note how this region corresponds with the region where apparent resistivities are accurate to within 10 percent in Figure 1.

In summary the half-space fields are different from the whole-space fields, but they should behave similarly with respect to the plane wave approximation. One difference is that the magnetic field in the whole-space is always linearly polarized, whereas the half-space magnetic field is linearly polarized only in the far-field. The electric field in both situations is elliptically polarized, becoming linearly polarized in the far-field. The angle between major axes of the electric and magnetic field polarization ellipses can be used as a measure of the validity of the far-field approximation. When the angle is within one degree of 90-degrees, the apparent resistivities using the magnetotelluric approximation are within 10 percent of the actual resistivity of the half-space.

APPENDIX C

EQUIPMENT USED IN THE FIELDWORK

Transmitter

The transmitter used in this survey was a Geotronics model EMT-5000 EM, IP, and AMT transmitter. It could transmit electric current at the following 16 fixed frequencies:

1.0005763 Hz	97.65625 Hz
2.9955905	212.585034
5.0080128	320.512821
7.026295	520.83
9.7656250	976.5625
21.345628	3205.128205
32.018443	5208.3333
82.236842	9803.92157

Only the ten highest frequencies were used in the CSAMT survey due to the limitations of the receiver.

The current transmitted was dependent upon the stake resistance. It was therefore necessary to minimize this resistance in order to maximize the signal. This was accomplished by using five electrodes in parallel at each end of the transmitter wire. Although the transmitter is capable of transmitting 20 amperes, we were unable to get more than about 8 amperes of current into the electrodes. At high frequencies the transmitted current was even less.

Receiver

The receiver used in this survey was a Kennecott Mark 5 AMT receiver designed by D. Green during 1966-67 and was on loan from Kennecott Copper Corp. The receiver is a tunable, high-gain, narrow band-pass system with two channels. The metered output is the logarithmic ratio (in decibels) of the two inputs. The measurement is therefore not the electric and magnetic fields, but a ratio of electric to magnetic fields, which is then used to calculate a scalar apparent resistivity according to the following equation.

$$\rho_a = \frac{1}{\mu\omega}\left(\frac{|E|}{|H|}\right)^2$$

The receiver is tuned manually to the transmitted frequencies. The lowest transmitted frequency able to be "tuned in" was 32.018443 Hz. This limited the depth of exploration of the survey.

The magnetic field sensor was a Kennecott Mark III ferrite-core, 12,000-turn coil, weighing about 23 lbs. We calibrated the coil by measuring its output when it was placed in the known magnetic field of a solenoid. A diagram of the calibration circuit is as follows:

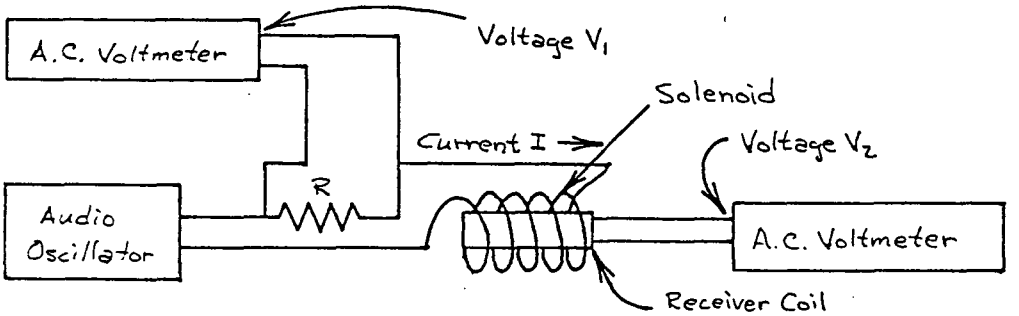

The magnetic field (H) in the solenoid is NI, where N is the number of turns per meter. Then, the coil sensitivity is

$$S_h = \frac{V_2}{H} = \frac{V_2}{NI} = \frac{V_2 R}{N V_1}$$

For the calibration done in this work, R=61.0 ohms, and N=100 turns/m.

Apparent Resistivity Calculation

The apparent resistivity is given by

$$\rho_a = \frac{1}{\mu\omega}\left(\frac{|E|}{|H|}\right)^2, \text{ where } \mu=\mu_0, \text{ and } \omega = 2\pi f$$

The voltage read on the electric field meter (V_e) is a product of the gain (G_e), the sensitivity of the electric field sensor (S_e), and the electric field strength (E). The magnetic field voltage is similarly $V_h=G_hS_hH$. Solving for E and H and plugging in the apparent resistivity equation,

$$\rho_a = \frac{1}{8\pi^2 f\times 10^{-7}}\left[\frac{V_e G_h S_h}{V_h G_e S_e}\right]^2$$

Then

$$10\log\rho_a = 10\log\left[\frac{1}{8\pi^2\times 10^{-7}}\right] - 10\log f + 20\log\frac{S_h}{S_e} + 20\log\frac{G_h}{G_e} + 20\log\frac{V_e}{V_h}$$

$$= 10\log\left[\frac{1}{8\pi^2\times 10^{-7}}\right] - 10\log f + S_h(db) - S_e(db) + G_h(db) - G_e(db) + \frac{V_e}{V_h}(db)$$

Now define

$$CF = 10\log\left[\frac{1}{8\pi^2\times 10^{-7}}\right] - 10\log f + S_h(db) - S_e(db)$$

Then

$$10\log\rho_a = \frac{V_e}{V_h}(db) + G_h(db) - G_e(db) + CF$$

The quantity S_e is the sensor voltage output per electric field strength. S_e is then just the receiver dipole length in meters which in this survey was 30.48 m (100 ft). S_h is the coil sensitivity which is determined for each frequency used. The values of S_h and CF determined in the laboratory were:

Coil	freq.	V_1	V_2	S_h	CF	COIL	V_1	V_2	S_h	CF
218	32.02Hz	.2V	1.15V	3.6	17.7	354	.1V	.57V	3.5	17.4
	82.24	.1	1.4	8.7	21.2		30mV	.435	9.0	21.5
	97.66	.08	1.27	9.8	21.8		30.	.51	10.5	22.1
	212.58	35mV	1.3	23.0	25.6		15.	.562	23.2	25.6
	320.51	20.	1.08	33.4	27.0		10.	.571	35.3	27.5
	520.83	13.	1.18	56.2	29.4		6.5	.61	58.1	29.7
	976.56	6.	1.1	113.5	32.8		2.5	.49	121.3	33.4
	3205.	.415	.415	85.6	25.2		3.	.34	70.1	23.4
	5208.	4.5	.3	41.3	16.7		4.5	.297	40.8	16.6
	9804.	10.	.214	13.2	4.1		10.	.185	11.5	2.9

The coil sensitivity versus frequency for coil 218 is plotted in Figure C1. The figure indicates the coil has a peak response at about 2 KHz.

A reading on the receiver consisted of recording the gains of the E and H channels, and the $|E|/|H|$ ratio. To get the apparent resistivity, the gain of the E channel (G_e) was subtracted from the gain of the H channel (G_h), and the ratio was added. The calibration factor (CF) was then added, the total was divided by 10, and the inverse logarithm to the base 10 was computed to give the apparent resistivity.

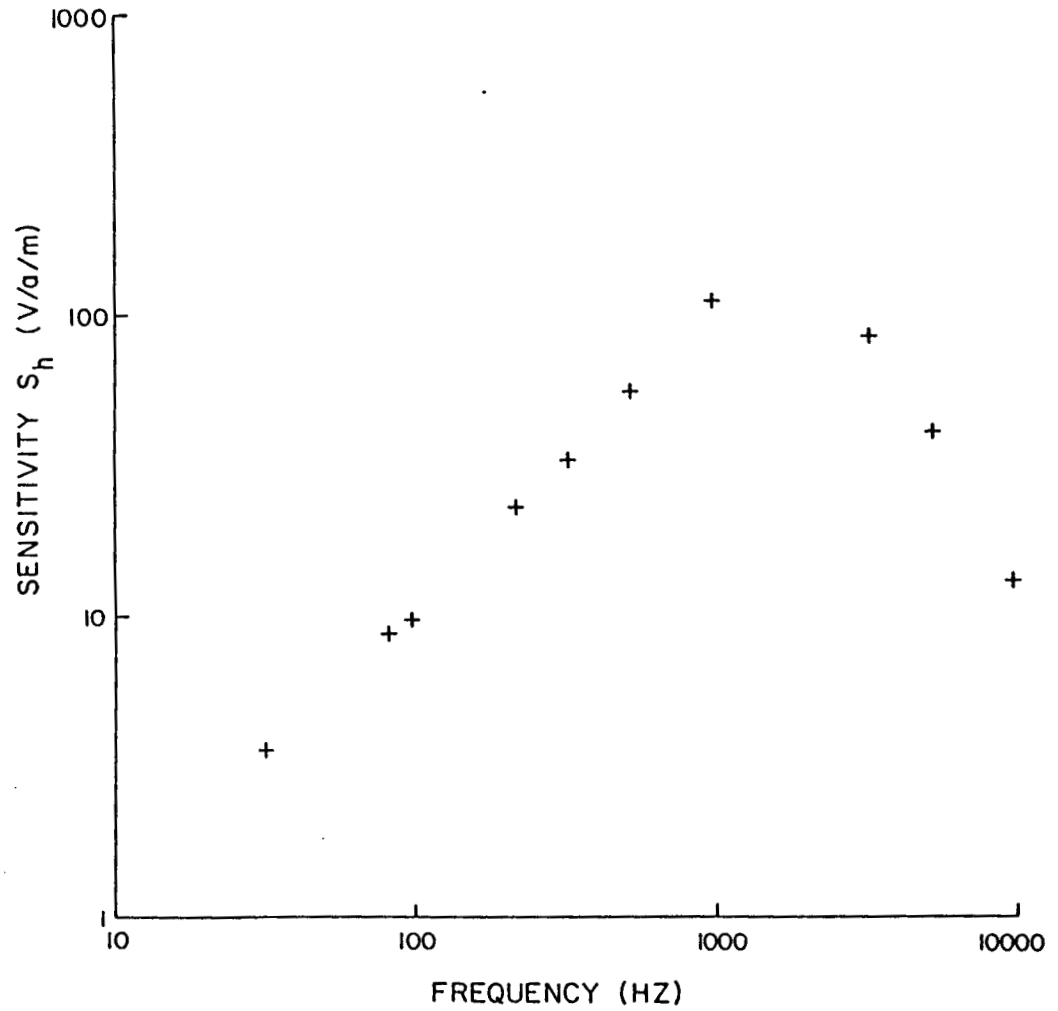

Figure C1. A plot of the coil sensitivity versus frequency for coil 218.

APPENDIX D

TABLE 3. REDUCED FIELD DATA

Station	Receiver	Coil	Latitude	Longitude	Transmitter	Apparent Resistivities 32	97.6	977.	5208
1	884	218	38°27.66'	112°52.62'	TX1	6.	14.	38.	37.
2	884	218	27.30°	52.74'	TX1	23.	18.	76.	148.
3	884	218	27.96'	52.54'	TX1	6.	22.	30.	30.
4a	884	218	27.30'	52.23'	TX1	23.	22.	76.	117.
5	884	218	26.64'	51.70'	TX1	1862.	447.	603.	589.
6a	884	218	27.09'	51.65'	TX1	1175.	355.	759.	741.
7	884	354	28.37'	52.94'	TX1	22.	41.	55.	115.
8	884	354	28.47'	52.67'	TX1	9.	22.	60.	74.
9	884	218	29.16'	51.76'	TX1	28.	16.	44.	115.
10	884	218	27.29'	51.58'	TX1	74.	89.	120.	186.
11	884	218	27.91'	51.13'	TX1	59.	56.	240.	295.
13-1	884	218	26.88'	55.18'	TX1	9.	28.	95.	117.
13-2	884	218	27.02'	54.98'	TX1	23.	35.	95.	117.
13-3	884	218	27.93'	53.62'	TX1	37.	45.	151.	186.

APPENDIX D - Continued

Station	Receiver	Coil	Latitude	Longitude	Transmitter	Apparent Resistivities 32	97.6	977.	5208
13-4	884	218	28.38'	53.55'	TX1	23.	35.	95.	186.
13-6	884	218	28.71'	53.56'	TX1	19.	35.	120.	117.
13-7	884	218	28.83'	52.27'	TX1	7.	18.	60.	47.
13-8	884	218	28.36'	52.29'	TX1	7.	18.	60.	74.
13-9	884	218	28.26'	52.07'	TX1	3.	2.	5.	7.
14-1	884	218	26.33'	51.71'	TX1	933.	224.	240.	148.
14-2	884	218	26.15'	52.00'	TX1	295.	141.	240.	148.
14-3	884	218	28.15'	51.08'	TX1	186.	141.	120.	117.
14-4	884	218	28.21'	51.54'	TX1	30.	56.	48.	74.
14-5	884	218	27.57'	51.91'	TX1	19.	18.	24.	30.
14-6	884	218	26.44'	55.82'	TX1	19.	14.	120.	186.
14-7	884	354	27.03'	55.79'	TX1	35.	-	138.	115.
14-8	884	354	27.75'	56.08'	TX1	35.	102.	219.	-
14-9	884	354	27.74'	54.98'	TX1	14.	51.	138.	288.
14-10	884	354	27.43'	54.33'	TX1	28.	65.	138.	182.

APPENDIX D - Continued

Station	Receiver	Coil	Latitude	Longitude	Transmitter	32	97.6	Apparent Resistivities 977.	5208.
14-11	884	354	26.40'	54.11'	TX1	35.	65.	275.	363.
15-3	884	354	30.22'	50.95'	TX2	5.	3.	3.	9.
15-4	884	354	30.51'	51.15'	TX2	9.	6.	2.	23.
15-5	884	354	30.94'	51.23'	TX2	28.	32.	28.	148.
15-6	884	354	31.09'	51.18'	TX2	28.	26.	44.	72.
15-7	884	354	30.99'	51.55'	TX2	14.	5.	87.	145.
15-8	884	354	30.61'	52.32'	TX2	9.	16.	44.	72.
15-9	884	354	30.53'	54.32'	TX2	17.	20.	87.	182.
17-1	884	354	29.48'	53.59'	TX2	-	-	110.	115.
17-2	884	354	29.07'	53.45'	TX2	22.	46.	87.	145.
17-3	884	354	29.15'	49.38'	TX2	-	-	1738	2884
17-4	884	354	29.57'	50.45'	TX2	44.	57.	110.	182.
17-5	884	354	29.69'	50.88'	TX2	22.	41.	55.	72.
17-6	884	354	29.52'	52.19'	TX2	22.	26.	69.	58.
17-7	884	354	29.52	52.73	TX2	22.	51.	87.	115.

APPENDIX D - Continued

Station	Receiver	Coil	Latitude	Longitude	Transmitter	Apparent Resistivities 32	97.6	977.	5208
18-1	884	354	29.48'	53.10'	TX2	28.	51.	110.	115.
18-2	884	354	29.93'	52.73'	TX2	28.	41.	69.	91.
18-3	884	354	29.80'	51.99'	TX2	17.	20.	55.	145.
18-4	884	354	29.05'	52.19'	TX2	28.	16.	55.	182.
19-1	884	354	29.16'	54.80'	TX2	14.	26.	87.	145.
19-2	884	354	29.73'	54.97'	TX2	17.	20.	69.	145.
19-3	884	354	28.77'	56.48'	TX2	14.	13.	44.	91.
19-4	884	354	29.70'	56.25'	TX2	14.	13.	44.	72.
19-5	884	354	31.10'	55.41'	TX2	9.	8.	35.	91.
19-6	884	354	30.55'	51.62'	TX2	3.	3.	9.	18.
19-7	884	354	30.74'	50.12'	TX2	55.	51.	69.	115.
19-8	884	354	30.74'	50.45'	TX2	7.	16.	35.	91.
19-9	884	354	31.14'	50.60	TX2	11.	-	28.	72.
19-10	805	354	31.51'	51.06'	TX2	-	-	35.	91.
19-11	805	354	30.60'	52.83'	TX2	14.	16.	28.	-

APPENDIX D - Continued

Station	Receiver	Coil	Latitude	Longitude	Transmitter	Apparent Resistivities 32.	97.6	977.	5208
19-12	805	354	30.59'	53.35'	TX2	22.	26.	28.	72.
19-13	805	354	28.71'	51.67'	TX2	17.	16.	17.	58.
19-14	805	354	29.33'	51.06'	TX2	17.	32.	28.	72.
19-15	805	354	28.80'	51.05'	TX2	69.	51.	87.	229.
19-16	805	354	28.44'	50.82'	TX2	275.	162.	138.	182.
20-1	805	354	28.94'	54.15'	TX2	17.	32.	69.	91.
20-2	805	354	28.15'	54.98'	TX2	17.	80.	87.	182.
20-3	805	218	27.99'	51.85'	TX2	15.	4.	8.	23.
20-4	805	218	28.11'	52.08'	TX2	30.	14.	15.	30.
20-5	805	218	29.30'	50.26'	TX2	93.	71.	76.	234.
20-6	805	218	29.53	48.85'	TX2	1862.	-	120.	74.
20-7	805	218	29.90'	50.88'	TX2	23.	28.	24.	47.
20-8	805	218	30.54'	50.78'	TX2	23.	7.	10.	19.
20-9	805	218	30.59'	51.94'	TX2	12.	9.	24.	37.
20-10	805	218	30.80'	51.90'	TX2	5.	9.	12.	15.

APPENDIX D - Continued

Station	Receiver	Coil	Latitude	Longitude	Transmitter	Apparent Resistivities 32.	97.6	977.	5208
20-11	805	218	29.14'	52.65'	TX2	12.	14.	30.	59.
21-1	805	218	29.83'	52.12'	TX2	15.	18.	38.	37.
21-2	805	218	30.74'	54.83'	TX2	12.	11.	30.	47.
21-3	805	218	30.75'	55.65'	TX2	7.	6.	15.	59.
21-4	805	218	32.01'	54.46'	TX2	19.	22.	38.	59.
21-5	805	218	31.86'	53.65'	TX2	19.	22.	38.	47.
21-6	805	218	31.74'	52.83'	TX2	19.	14.	19.	47.
21-7	805	218	31.42'	52.10'	TX2	12.	7.	15.	30.
30-1	805	218	29.87'	53.61'	TX3	12.	14.	38.	37.
30-2	805	218	30.21'	53.63'	TX3	30.	45.	95.	117.
31-1	805	218	30.16'	54.59'	TX3	15.	18.	60.	117.
31-2	8L5	218	28.62'	54.97'	TX3	12.	22.	48.	74.
9-1	805	218	26.84'	52.93'	TX5	23.	35.	95.	93.
9-2	805	218	26.47'	53.13	TX5	30.	38.	76.	117.
9-3	805	218	26.00'	53.01'	TX5	37.	282.	-	59.

Profile 1 Latitude 38°29.48'

Data on Pseudosections Receiver 805 Coil 218

Station	Longitude	Trans.	Station	Longitude	Trans.
900	112°54.35'	TX3	4200	112°52.09'	TX4
1200	54.15'	TX3	4500	51.88'	TX4
1500	53.93'	TX3	4800	51.68'	TX4
1800	53.73'	TX3	4950	51.57'	TX4
2100	53.52'	TX3	5100	51.46'	TX4
2400	53.31'	TX3	5400	51.25'	TX4
2700	53.14'	TX3	5700	51.07'	TX4
3000	52.93'	TX3	6000	50.86'	TX4
3300	52.72'	TX3	6300	50.65'	TX4
3600	52.51'	TX3	6600	50.44'	TX4
3900	52.30'	TX3	6900	50.24'	TX4
			7200	50.03'	TX4

Profile 2 Latitude 38°28.49'

Data on Pseudosections Receiver 805 Coil 218

Station	Longitude	Trans.	Station	Longitude	Trans.
3000 W	112°54.87'	TX5	600 E	112°52.37'	TX4
2700 W	54.66'	TX5	900 E	52.15'	TX5
2400 W	54.45'	TX5	1200 E	51.99'	TX5
2100 W	54.24'	TX5	1500 E	51.78'	TX5
1800 W	54.04'	TX5	1800 E	51.56'	TX5
1500 W	53.82'	TX5	2100 E	51.35'	TX5
1200 W	53.62'	TX5	2400 E	51.15'	TX5
900 W	53.41'	TX5	2700 E	50.93'	TX5
600 W	53.20'	TX4	3000 E	50.72'	TX5
300 W	52.99'	TX4	3300 E	50.51'	TX5
0	52.79'	TX4	3600 E	50.31'	TX5
300 E	52.58'	TX4	3900 E	50.10'	TX5

APPENDIX E

REPEATED STATIONS AND TESTS BETWEEN RECEIVERS

Data from receiver sites which were repeated, and sites where our field equipment was tested, are listed below. Two receivers and two coils were used. High and low values of apparent resistivity (rho) correspond to one decibel higher or lower in the E/H ratio read on the receiver. The spread or difference in decibels means that the E/H measurements used to compute apparent resistivity ranged over that many decibels.

Station 2 -- Both coils and both receivers -- Transmitter TX1

freq.	receiver	coil	rho	(high, low)	spread in db
32.02	884	354	11.	(14,9)	
		218	23.	(29,19)	
	805	354	17.	(22,14)	
		218	19.	(23,15)	4
82.24	884	354	28.	(35,22)	
		218	26.	(33,21)	
	805	354	2.	(3,2)	
		218	2.	(3,2)	11
97.66	884	354	32.	(41,26)	
		218	18.	(22,14)	
	805	354	26.	(32,20)	
		218	28.	(35,22)	2
212.58	884	354	46.	(57,36)	
		218	57.	(72,46)	
	805	354	36.	(46,29)	
		218	57.	(72,46)	2
320.51	884	354	71.	(89,56)	
		218	63.	(79,50)	
	805	354	45.	(56,35)	
		218	40.	(50,32)	2
520.83	884	354	60.	(74,47)	
		218	87.	(110,69)	

	805	354	47.	(59,37)	
		218	69.	(87,55)	3
976.56	884	354	138.	(174,110)	
		218	76.	(95,60)	
	805	354	55.	(69,44)	
		218	48.	(60,38)	4
3205.	884	354	87.	(110,69)	
		218	83.	(105,66)	
	805	354	69.	(87,55)	
		218	52.	(66,42)	4
5208.	884	354	182.	(229,144)	
		218	148.	(186,117)	
	805	354	72.	(91,57)	
		218	59.	(74,47)	5
9804.	884	354	98.	(123,78)	
		218	162.	(204,129)	
	805	354	62.	(78,49)	
		218	81.	(102,65)	3

Station 17-6 -- Both coils -- Transmitter TX2 -- Receiver 884

freq.	coil	rho	(high, low)	diff. in db
32.02	354	22.	(27,17)	
	218	29.	(37,23)	1
97.66	354	26.	(32,20)	
	218	28.	(35,22)	1
976.56	354	69.	(87,55)	
	218	76.	(95,60)	1
5208.	354	57.	(72,46)	
	218	74.	(93,59)	1

Station 2400 (N-S) -- Both receivers -- Transmitter TX3 -- Coil 218

freq.	receiver	rho	(high, low)	diff. in db
9804.	805	51.	(65,41)	
	884	41.	(51,32)	1
5208.	805	59.	(74,47)	
	884	74.	(93,59)	1
3205.	805	66.	(83,52)	
	884	105.	(132,83)	2
976.56	805	48.	(60,38)	
	884	76.	(95,60)	2
520.83	805	44.	(55,35)	
	884	69.	(87,55)	2
320.51	805	32.	(40,25)	
	884	40.	(50,32)	1
212.58	805	29.	(36,23)	
	884	72.	(91,57)	4
97.66	805	18.	(22,14)	
	884	35.	(45,28)	3
82.24	805	17.	(21.13)	
	884	33.	(42,36)	3
32.02	805	29.	(37,23)	
	884	23.	(29,19)	1

Repeat Stations

Station 13-6 -- Rec 884
Coil 218
TX1

freq.	rho	(high, low)
32.02	19.	(23,15)
97.66	35.	(45,28)
976.56	120.	(151,95)
5208.	117.	(148,93)

Station 15-1 -- Rec 884
Coil 354
TX2

rho	(high, low)	diff. in db
14.	(17,11)	1
32.	(41,26)	1
87.	(110,69)	2
144.	(182,115)	1

Station 15-2 -- Rec 884
Coil 354
TX2

freq.	rho	(high, low)
32.02	37.	(47,29)
97.66	--	-------
976.56	30.	(38,24)
5208.	74.	(93,59)

Station 9 -- Rec 884
Coil 218
TX1

rho	(high, low)	diff. in db
27.	(35,22)	1
16.	(20,13)	--
44.	(55,35)	1
115.	(144,91)	2

Station 17-7 -- Rec 884
Coil 354
TX2

freq.	rho	(high, low)
32.02	22.	(27,27)
97.66	51.	(65,41)
976.56	87.	(110,69)
5208.	115.	(144,91)

Station 3300 -- Rec 805
Coil 218
TX3

rho	(high, low)	diff. in db
23.	(29,19)	0
45.	(56,35)	0
38.	(48,30)	3
47.	(59,37)	4

		Station 4200A -- TX3		Station 4200B -- TX4		
		Rec 805 -- Coil 218		Rec 805 -- Coil 218		
freq.	E-field orientation	rho	(high,low)	rho	(high,low)	diff.in db
98.04	N-S	41.	(51,32)	51.	(65,41)	1
	E-W	65.	(81,51)	65.	(81,51)	0
5208.	N-S	74.	(93,59)	37.	(47,29)	3
	E-W	47.	(59,37)	47.	(59,37)	0
3205.	N-S	52.	(66,42)	42.	(52,33)	1
	E-W	52.	(66,42)	42.	(52,33)	1
976.56	N-S	48.	(60,38)	30.	(38,24)	2
	E-W	30.	(38,24)	30.	(38,24)	0
520.83	N-S	44.	(53,35)	44.	(55,35)	0
	E-W	44.	(55,35)	35.	(44,27)	1
320.51	N-S	40.	(50,32)	40.	(50,32)	0
	E-W	32.	(40,25)	40.	(50,32)	1
212.58	N-S	46.	(57,36)	57.	(72,46)	1
	E-W	36.	(46,29)	36.	(46,29)	0
97.66	N-S	22.	(28,18)	28.	(35,22)	1
	E-W	22.	(28,18)	22.	(28,18)	0
82.24	N-S	21.	(26,17)	26.	(33,21)	1
	E-W	17.	(21,13)	26.	(33,21)	2
32-02	N-S	23.	(29,19)	29.	(37,23)	1
	E-W	59.	(74,47)	47.	(59,37)	1

Conclusions

The data from station 2 suggests a considerable variance in apparent resistivity. When only the coils are interchanged as in stations 17-6, the variance is down to one decibel. Station 2400 shows larger variances leading to the conclusion that there is a detectably large difference in using both receivers. Repeat stations are usually good to within one decibel except when two different receivers are used as in stations 17-7 and 3300. Station 4200 confirms low errors when the same receiver is used along with the same coil. (See Figure E1)

These comparisons show that there may be a considerable variance in the data in the overall resistivity mapping, but the profile data is generally good to one decibel of difference in the ratio E/H.

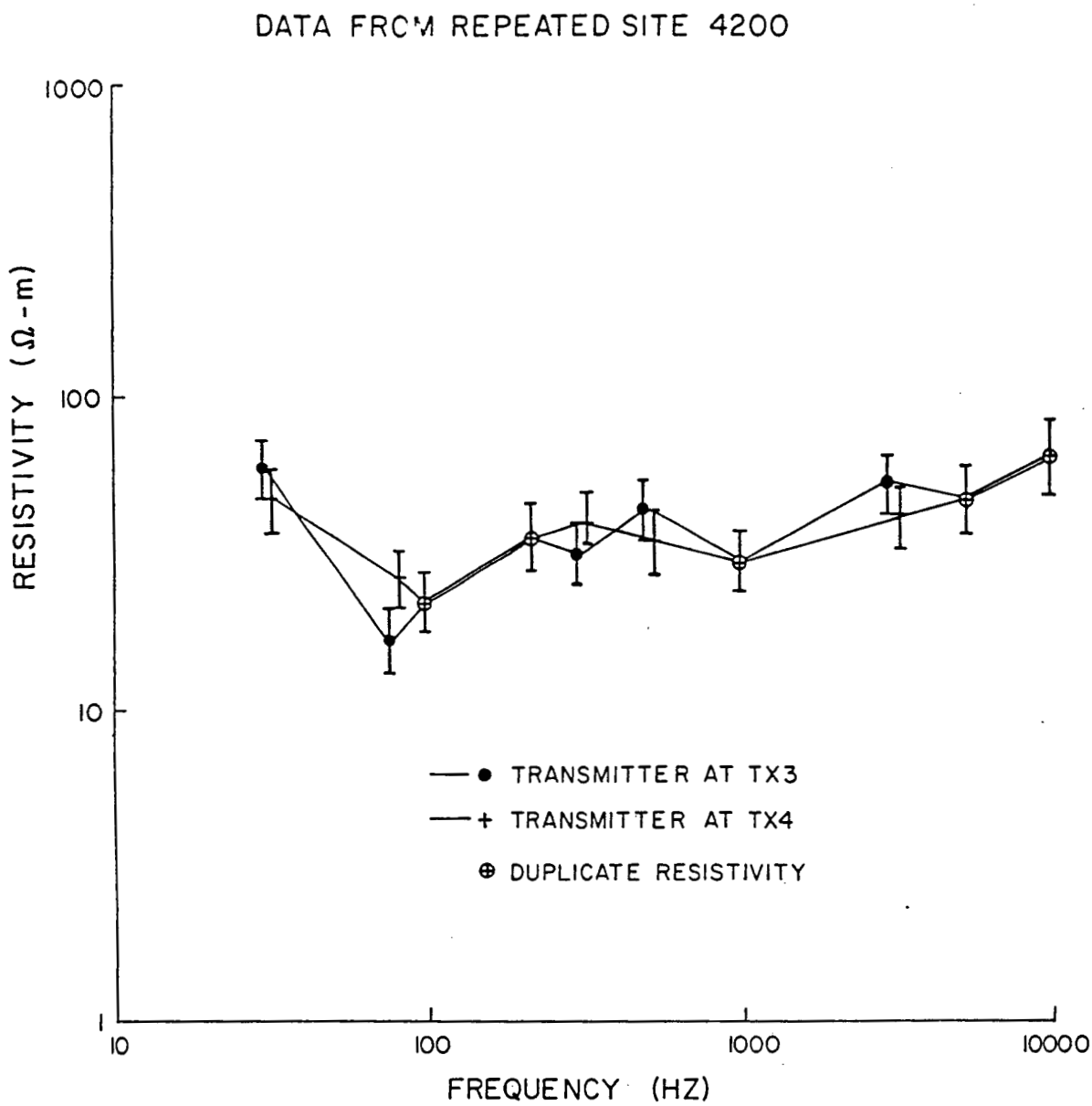

Figure E1. A plot of apparent resistivity versus frequency for station 4200. Showing repeatability when two different transmitter sites were used. The error bars correspond to one decibel higher or lower in the ratio E/H read on the receiver.

MT Site Reoccupied

The absolute accuracy of the resistivities obtained by our equipment was checked by re-occupying a magnetotelluric site. We occupied a site used in 1976 by Geotronics Corp. survey which was 2200 meters east of transmitter TX2. Assuming the maximum resistivity to be 60 ohm-m, this station is 3.2 skin depths away from the transmitter at 32.02 Hz. Apparent resistivities obtained by the two methods are plotted in Figure E2.

The CSAMT data merges with the MT data indicating that the equipment was working properly and apparent resistivities obtained are accurate.

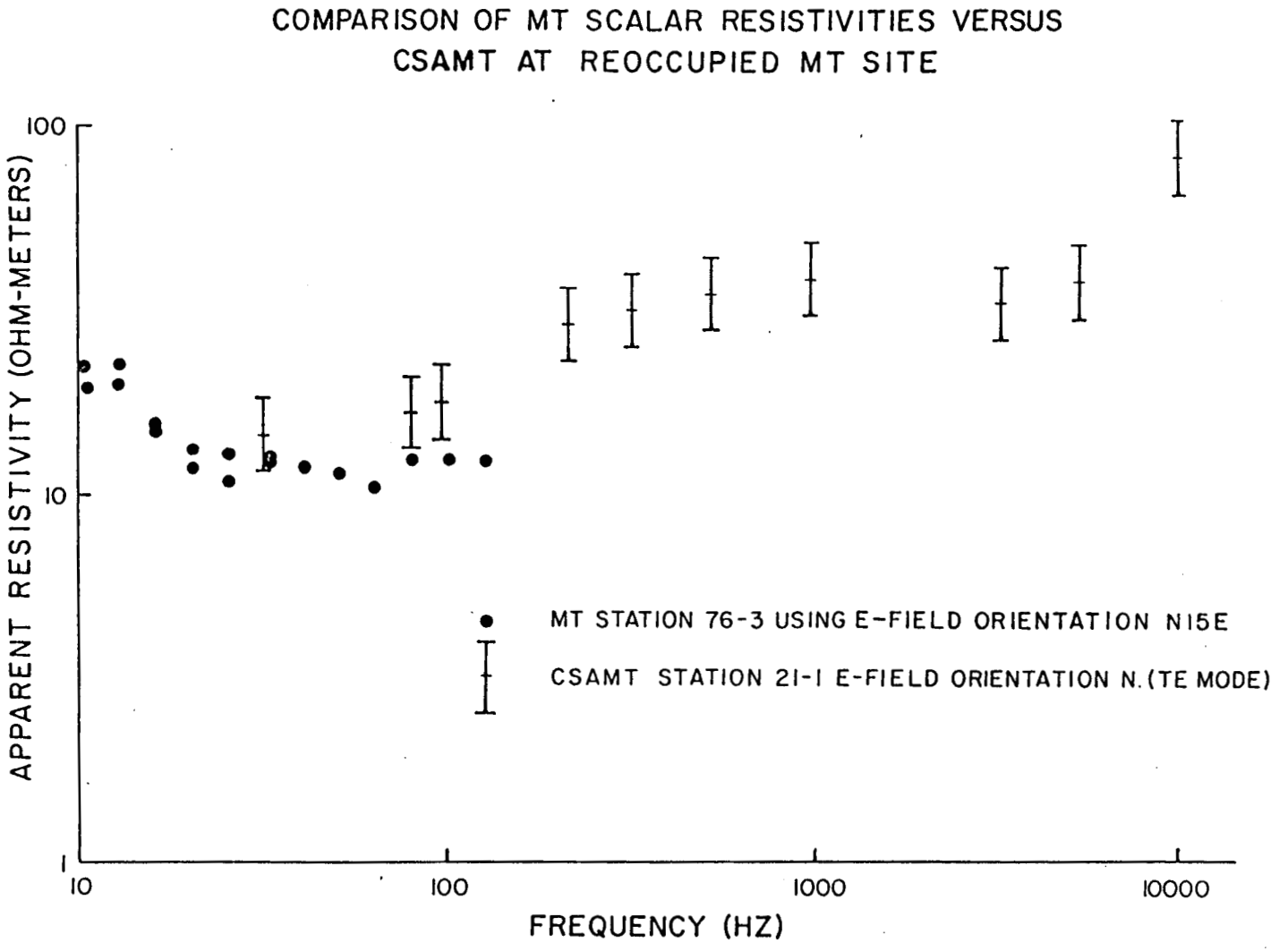

Figure E2. Apparent resistivity versus frequency for reoccupied magnetotelluric site. MT data are scalar apparent resistivities with the electric field orientation N15E.

REFERENCES

Crebs, T. L., 1976, Gravity and ground magnetic surveys of the central Mineral Mountains, Utah: M. S. Thesis, Department of Geology and Geophysics, Univ. of Utah.

Glenn, W. E., and Hulen, J. B., 1979, Interpretation of well log data from four drill holes at Roosevelt Hot Springs KGRA: Univ. of Utah Research Inst., Earth Science Laboratory Rept. 28, DOE/DGE Contract EG-78-C-07-1701.

Goldstein, M. A., and Strangway, D. W., 1975, Audio frequency magnetotellurics with a grounded electric dipole source: Geophysics, v. 40, p. 669-683.

Harrington, R. F., 1961, Time-harmonic electromagnetic fields: New York, McGraw-Hill, 480 p.

Hoover, D. B., Frischknecht, F. C., and Tippens, C., 1976, Audio-magnetotelluric soundings as a reconnaissance exploration technique in Long Valley, Calif.: J. Geophys. Res., v. 81, p. 801-809.

Hoover, D. B., and Long, C. L., 1976, Audio-magnetotelluric methods in reconnaissance geothermal exploration: Proc. 2nd U.N. Sympos. Devel. Geothermal Resources, p. 1059-1064.

Hoover, D. B., Long, C. L., and Senterfit, R. M., 1978, Some results from audiomagnetotelluric investigations in geothermal areas: Geophysics, v. 43, p. 1501-1514.

Hohmann, G. W., 1975, Three-dimensional induced polarization and electromagnetic modeling: Geophysics, v. 40, p. 309-324.

Kan, T., and Clay, C. S., 1979, Hybrid-ray approximation in electromagnetic sounding: Geophysics, v. 44, p. 1846-1861.

Killpack, T. J., and Hohmann, G. W., 1979, Interactive dipole-dipole resistivity and IP modeling of arbitrary two-dimensional structures (IP2D users guide and documentation): Univ. of Utah Research Inst., Earth Science Laboratory Rept. 15, DOE/DGE Contract EG-78-C-07-1701.

Long, C. L., and Kaufmann, H. E., 1980, Reconnaissance geophysics of a known geothermal resource area, Weiser, Idaho, and Vale, Oregon: Geophysics, v. 45, p. 312-322.

Nielson, D. L., Sibbett, B. S., McKinney, D. B., Hulen, J. B., Moore, J. N., Samberg, S. M., 1978, Geology of Roosevelt Hot Springs KGRA, Beaver County, Utah: Univ. of Utah Research Inst., Earth Science Laboratory Rept. 12, DOE/DGE Contract EG-78-C-07-1701.

Ross, H. P., Nielson, D. L., Smith, C., Glenn, W. E., Moore, J. N., and Fox, R. C., 1980, An integrated case study of the Roosevelt Hot Springs KGRA, Beaver County, Utah: Univ. of Utah Research Inst., Earth Science Laboratory, DOE/DGE Contract EG-78-C-07-1701, In Preparation.

Roy, A., and Apparao, A., 1971, Depth of investigation in direct current methods: Geophysics, v. 36, p. 943-959.

Stodt, J. A., 1978, Documentation of a finite element program for solution of geophysical problems governed by the inhomogeneous 2-D scalar helmholtz equation: NSF grant AER-11155, Univ. of Utah, 66 p.

Strangway, D. W., Swift, C. M., and Holmer, R. C., 1973, The application of audio-frequency magnetotellurics (AMT) to mineral exploration: Geophysics, v. 38, p. 1159-1175.

Tripp, A. C., 1977, Electromagnetic and Schlumberger resistivity sounding in the Roosevelt Hot Springs Known Geothermal Resource Area: M. S. Thesis, Department of Geology and Geophysics, Univ. of Utah.

Tripp, A. C., and Hohmann, G. W., 1980, Group theoretic reduction of impedance matrix dimension in three dimensional integral equations electromagnetic modeling in geophysics: Unpublished manuscript.

Wannamaker, P. E., Ward, S. H., Hohmann, G. W., and Sill, W. R., 1980, Magnetotelluric models of the Roosevelt Hot Springs, Utah, KGRA: In preparation.

Ward, S. H., and Sill, W. R., 1976, Dipole-dipole resistivity surveys, Roosevelt Hot Springs KGRA: NSF final rep., v. 2, grant GI-43741, Univ. of Utah, 29 p.

Ward, S. H., Parry, W. T., Nash, W. P., Sill, W. R., Cook, K. L., Smith, R. B., Chapman, D. S., Brown, F. H., Whelan, J. A., and Bowman, J. R., 1978, A summary of the geology, geochemistry, and geophysics of the Roosevelt Hot Springs thermal area, Utah: Geophysics, v. 43, p. 1515-1542.